The Astrophysical Journal, 977:152 (27pp), 2024 December 20 https://doi.org/10.3847/1538-4357/ad8cd3

SN 2021foa: The "Flip-flop" Type IIn/Ibn Supernova

D. Farias[1], C. Gall[1], G. Narayan[2], S. Rest[3], V. A. Villar[4,5], C. R. Angus[1,6], K. Auchettl[7,8], K. W. Davis[7], R. J. Foley[7], A. Gagliano[4,5,9], J. Hjorth[1], L. Izzo[1,10], C. D. Kilpatrick[11], H . M. L. Perkins[2], E. Ramirez-Ruiz[7], C. L. Ransome[4], A. Sarangi[1], R. Yarza[7], D. A. Coulter[12], D. O. Jones[13], N. Khetan[14], A. Rest[3,12], M. R. Siebert[12], J. J. Swift[15], K. Taggart[7], S. Tinyanont[7,16], P. Wrubel[15], T. J. L. de Boer[17], K. E. Clever[7], A. Dhara[7], H. Gao[17], and C.-C. Lin[17]

[1] DARK, Niels Bohr Institute, University of Copenhagen, Jagtvej 128, 2200 Copenhagen, Denmark; diego.farias@nbi.ku.dk
[2] Department of Astronomy, University of Illinois at Urbana-Champaign, 1002 W. Green Street, IL 61801, USA
[3] Department of Physics and Astronomy, The Johns Hopkins University, Baltimore, MD 21218, USA
[4] Harvard-Smithsonian Center for Astrophysics, 60 Garden Street, Cambridge, MA 02138, USA
[5] The NSF AI Institute for Artificial Intelligence and Fundamental Interactions, USA
[6] Astrophysics Research Centre, School of Mathematics and Physics, Queen's University Belfast, Belfast BT7 1NN, UK
[7] Department of Astronomy and Astrophysics, University of California, Santa Cruz, CA 95064, USA
[8] School of Physics, The University of Melbourne, Melbourne, VIC 3010, Australia
[9] Department of Physics, Massachusetts Institute of Technology, Cambridge, MA 02139, USA
[10] INAF-Osservatorio Astronomico di Capodimonte, Salita Moiariello 16, I-80121, Naples, Italy
[11] Center for Interdisciplinary Exploration and Research in Astrophysics (CIERA) and Department of Physics and Astronomy, Northwestern University, Evanston, IL 60208, USA
[12] Space Telescope Science Institute, Baltimore, MD 21218, USA
[13] Institute for Astronomy, University of Hawaii, 640 N. A'ohoku Place, Hilo, HI 96720, USA
[14] School of Mathematics and Physics, The University of Queensland, Brisbane, QLD 4072, Australia
[15] The Thacher School, 5025 Thacher Road, Ojai, CA 93023, USA
[16] National Astronomical Research Institute of Thailand, Chiang Mai, Thailand
[17] Institute for Astronomy, University of Hawaii, 2680 Woodlawn Drive, Honolulu, HI 96822, USA
Received 2024 August 30; revised 2024 October 25; accepted 2024 October 25; published 2024 December 10

Abstract

We present a comprehensive analysis of the photometric and spectroscopic evolution of SN 2021foa, unique among the class of transitional supernovae for repeatedly changing its spectroscopic appearance from hydrogen-to-helium-to-hydrogen dominated (IIn-to-Ibn-to-IIn) within 50 days past peak brightness. The spectra exhibit multiple narrow ($\approx$300–600 km s^{-1}) absorption lines of hydrogen, helium, calcium, and iron together with broad helium emission lines with a full width at half-maximum (FWHM) of $\sim$6000 km s^{-1}. For a steady, wind mass-loss regime, light-curve modeling results in an ejecta mass of $\sim 8\,M_{\odot}$ and circumstellar material (CSM) mass below 1 $M_{\odot}$, and an ejecta velocity consistent with the FWHM of the broad helium lines. We obtain a mass-loss rate of $\approx 2\,M_{\odot}$ yr^{-1}. This mass-loss rate is 3 orders of magnitude larger than derived for normal Type II supernovae. We estimate that the bulk of the CSM of SN 2021foa must have been expelled within half a year, about 12 yr ago. Our analysis suggests that SN 2021foa had a helium-rich ejecta that swept up a dense shell of hydrogen-rich CSM shortly after explosion. At about 60 days past peak brightness, the photosphere recedes through the dense ejecta-CSM region, occulting much of the redshifted emission of the hydrogen and helium lines, which results in an observed blueshift (~ -3000 km s^{-1}). Strong mass-loss activity prior to explosion, such as those seen in SN 2009ip-like objects and SN 2021foa as precursor emission, are the likely origin of a complex, multiple-shell CSM close to the progenitor star.

Unified Astronomy Thesaurus concepts: Stellar mass loss (1613); Supernovae (1668); Core-collapse supernovae (304)

Materials only available in the online version of record: data behind figures, machine-readable table

1. Introduction

Massive stars ($\gtrsim 8\,M_{\odot}$) undergo different mass-loss phases, losing material from their outer layers shortly before core collapse (CC; S. J. Smartt 2009; N. Smith 2017). Analysis of this expelled material, termed circumstellar material (CSM), can provide important information about the progenitor system, and thus, the late stage of massive stellar evolution (see, e.g., V. Morozova et al. 2018). The CSM surrounds the progenitor, and thus, the supernova (SN) radiation and ejecta inevitably interact with the CSM. The emanating signatures arising from the interaction appear at a variety of phases during the evolution of the SN, depending primarily upon the mass distribution of the CSM (L. Dessart & D. J. Hillier 2022). This interaction produces SN spectra that can be dominated by narrow ($\sim$100–500 km s^{-1}) or intermediately broad ($\sim$1000 km s^{-1}) emission lines and P Cygni profiles (see M. Fraser 2020, and references therein).

Depending upon the progenitor system, as well as the composition and radial distribution of the CSM, different classes of core-collapse supernovae (CCSNe) have been identified.

CCSNe with a hydrogen (H)-rich CSM and little helium (He) emission in their spectra are commonly classified as Type IIn supernovae (SNe IIn; E. M. Schlegel 1990). Classical examples

of such events are, e.g., SN 1998S, SN 2005ip, and SN 2010jl (O. Fox et al. 2009; J. Mauerhan & N. Smith 2012; C. Fransson et al. 2014; C. Gall et al. 2014). However, if the CSM is He-rich with little-to-no H emission in the SN spectra, then the CCSNe are classified as Type Ibn supernovae (SNe Ibn; R. J. Foley et al. 2007; A. Pastorello et al. 2007). In recent years, another class of interacting SNe has emerged, the Type Icn supernovae (SNe Icn; A. Gal-Yam et al. 2022; C. Pellegrino et al. 2022; K. W. Davis et al. 2023). These SNe exhibit narrow oxygen (O) and carbon (C) emission lines in their spectra.

In the local universe, SNe IIn and Ibn comprise about 5% and 1% of the volumetric rate of CCSNe, respectively (K. Maeda & T. J. Moriya 2022; C. Cold & J. Hjorth 2023). Among the interacting CCSNe, SNe Icn are the rarest, with only five members known thus far (see K. W. Davis et al. 2023). However, the classification of several interacting SNe is ambiguous, as some CCSNe appear to change their type, e.g., from SNe IIn to Ibn or vice versa. Prominent examples are SN 2005la (A. Pastorello et al. 2008b), SN 2011hw (N. Smith et al. 2012a; A. Pastorello et al. 2015a), iPTF15akq (G. Hosseinzadeh et al. 2017), and SN 2020bqj (E. C. Kool et al. 2021). These objects form the unique group of transitional SNe IIn/Ibn.

Determining the exact nature of the progenitor of interacting SNe is challenging due to the complexities of the interaction between the ejecta and the CSM. Thus, SNe IIn have diverse light curves, spanning a broad range of peak magnitudes (A. Nyholm et al. 2020) and light-curve shapes. This has led to suggest a wide range of plausible progenitors systems for SNe IIn, such as red supergiants (RSG) in binary systems (SN 1998S-like objects; N. Smith 2017), luminous blue variables (LBVs), e.g., for SN 2005gl (A. Gal-Yam et al. 2007), SN 2009ip (R. J. Foley et al. 2011; N. Smith et al. 2013), SN 2010jl (N. Smith et al. 2011), and SN 2015bh (I. Boian & J. H. Groh 2018), while an $\sim 20\,M_{\odot}$ star is preferred for SN 2016jbu (C. D. Kilpatrick et al. 2018; S. J. Brennan et al. 2022a). The progenitor of SN 2015bh is also proposed to be a yellow supergiant ($\sim 50\,M_{\odot}$) (C. C. Thöne et al. 2017).

On the contrary, the light curves of SNe Ibn show a high degree of homogeneity (G. Hosseinzadeh et al. 2017). Thus, the most plausible progenitor is an an evolved Wolf–Rayet (W-R) star (A. Pastorello et al. 2008a), which is consistent with the majority of Ibn SNe being found in star-forming galaxies (although see PS1-12sk; G. Hosseinzadeh et al. 2019). Furthermore, the mass-loss rates derived from light-curve modeling of, e.g., OGLE-2014-SN-131 and SN 2020bqj (e.g., E. Karamehmetoglu et al. 2017; E. C. Kool et al. 2021) favor such a progenitor. Alternatively, SNe Ibn may be the explosion of a low-mass helium star in a binary system (L. Dessart et al. 2022). Unlike SNe IIn (see SN 2005gl; A. Gal-Yam et al. 2007), there is no detection of any progenitor system of SNe Ibn in archival data. However, late-time photometry at the location of SN 2006jc has shown a potential companion associated with the exploding star (J. R. Maund et al. 2016; N.-C. Sun et al. 2020).

A handful of CCSNe exhibited pre-explosion activities or outbursts up to two decades prior to their terminal explosion. Precursor emission in SNe IIn is common (e.g., J. C. Mauerhan et al. 2013; E. O. Ofek et al. 2013b; N. Elias-Rosa et al. 2016; C. C. Thöne et al. 2017; A. Pastorello et al. 2018; D. Hiramatsu et al. 2024), such as the case of SN 2009ip (A. Pastorello et al. 2013; R. Margutti et al. 2014). This transient was first classified as an SN impostor (e.g., R. J. Foley et al. 2011). However, after two more outbursts in 2011 and 2012, its "final" rebrightening in 2012 reached $M_R \approx -18$ mag, which was proposed as the terminal explosion of an SN IIn (J. C. Mauerhan et al. 2013). On the contrary, precursor emission has only been observed for three SNe Ibn: 2006jc (R. J. Foley et al. 2007), 2019uo (N. L. Strotjohann et al. 2021), and 2023fyq (S. J. Brennan et al. 2024a; Y. Dong et al. 2024).

Interacting SNe with observed signatures of pre-explosion outbursts and a photometric and spectroscopic evolution similar to that of SN 2009ip are termed 2009ip-like objects (A. Pastorello et al. 2018; S. J. Brennan et al. 2022b). Prominent examples of this class include SN 2015bh (N. Elias-Rosa et al. 2016; C. C. Thöne et al. 2017), SN 2016jbu (C. D. Kilpatrick et al. 2018; S. J. Brennan et al. 2022b), and SN 2019zrk (C. Fransson et al. 2022). Typically, photometric and spectroscopic data obtained around the epochs of the outbursts suggest that these are LBV-like eruptions prior to the presumed terminal explosion of the progenitor (A. Pastorello et al. 2013; C. C. Thöne et al. 2017; S. J. Brennan et al. 2022a). However, whether or not the latter are indeed stellar explosions remains unclear (N. Smith et al. 2022).

Here, we present unpublished multiband photometry and time-series spectroscopy of the fifth transitional SNe IIn/Ibn 2021foa. The data were collected by the Young Supernova Experiment (D. O. Jones et al. 2021; P. D. Aleo et al. 2023; D. A. Coulter et al. 2023). The SN (R.A. = 13:17:12.29, decl. = −17:15:24.19) was discovered by ASAS-SN (K. Z. Stanek & C. S. Kochanek 2021) on 2021 March 15 ($g \sim 15.9$) in the galaxy IC 086 (ASAS-SN-21dg). It was initially classified as an SNe IIn due to the strong, narrow Balmer lines in the optical spectrum (C. Angus 2021). An analysis of its light curve and spectra until +79 days (A. Reguitti et al. 2022) suggests that SN 2021foa is photometrically similar to SN 2009ip-like objects such as SN 2005gl (A. Gal-Yam et al. 2007), SN 2009ip (A. Pastorello et al. 2013), and notably, SN 2016jbu (C. D. Kilpatrick et al. 2018; S. J. Brennan et al. 2022b), while spectroscopically resembles the transitional SNe IIn/Ibn. In this work, we present a comprehensive analysis of the spectroscopic and photometric evolution out to +427 days. We detail a physical picture of this unusual SN, which, among its counterparts in the 2009ip-like class, exhibits some unique characteristics.

We determine the time of maximum light in the r band using a second-degree polynomial fit between MJD 59280 and 59315 to be $\mathrm{MJD_{max}} = 59302.35 \pm 0.14$ (r_{max}). We use this as our reference time throughout the remainder of the paper. Throughout this work, we assume a standard ΛCDM cosmology with $H_0 = 67.8\,\mathrm{km\,s^{-1}\,Mpc^{-1}}$ and $\Omega_m = 0.307$ (Planck Collaboration et al. 2014).

The paper is structured as follows: Section 2 describes the data acquisition and reduction. In Section 3, we present our photometric and spectroscopic analysis methodology, with the results presented in Section 4. We discuss our results from the analysis in Section 5, and conclude by formulating a complete physical scenario for SN 2021foa in Section 6.

2. Observations

Our photometric and spectroscopic follow-up observations of SN 2021foa, including archival and public data, are described below.

2.1. Photometric Data

We obtained optical photometry with the Sinistro imagers on the Las Cumbres Observatory (LCO) 1 m telescope network (T. M. Brown et al. 2013) in the *UBVRI*, *up*, *gp*, *rp*, *ip*, *z* bands, starting 2021 March 15 through 2021 August 17. Initial automatic processing of the imaging data, including instrument signature removal, pixel-level corrections, and astrometric calibration, was performed by the LCO `BANZAI` pipeline (C. McCully et al. 2018). Thereafter, images were processed using the `PhotPipe` pipeline (A. Rest et al. 2005; D. O. Jones et al. 2021). We measured the flux of SN 2021foa from the LCO images using an updated version of `DoPhot` (P. L. Schechter et al. 1993), and this photometry was calibrated using *u*-band Sloan Digital Sky Survey (S. Alam et al. 2015) together with *griz* Pan-STARRS1 photometric standards observed in the vicinity of SN 2021foa. We calibrated the photometry of the *R* and *I* bands on the Cousins photometric system.

Observations with the Ultraviolet and Optical Telescope (UVOT; P. W. A. Roming et al. 2005) on board the Neil Gehrels Swift Observatory were reported in A. Reguitti et al. (2022). UVOT data of SN 2021foa were taken between 2021 March 16 and 2021 May 10. Following the methodology described in P. J. Brown et al. (2014), we use `uvotsource` from the `HEASoft v6.26` package to perform aperture photometry within a 3″ aperture centered on SN 2021foa. We measured the total background flux at the location of SN 2021foa from frames obtained on 2022 June 17, when any residual light from the fading SN is well below the sky background. The background emission was then subtracted from all previous observations. We detected emissions of SN 2021foa at a $>3\sigma$ level in all UVOT bands in the 2021 observations.

SN 2021foa was also observed by the Asteroid Terrestrial-impact Last Alert System (ATLAS; J. L. Tonry et al. 2018) between February 22 to July 16 and March 20 to July 14 in the *o* and *c* bands, respectively. Following the procedure described by K. W. Davis et al. (2023), we obtained the binned light-curve data calculated as a 3σ cut weighted mean for each night. In contrast to A. Reguitti et al. (2022, 2024), we did not find any significant detection in the *c* band prior to February 22 (see Appendix B).

Additional images of SN 2021foa were obtained in the *BVri* bands with the 1 m Nickel telescope at Lick Observatory and in the *up*, *gp*, *rp*, *zp* bands with the Thacher 0.7 m telescope in Ojai, CA (J. J. Swift et al. 2022). The images from the Nickel telescope were calibrated using bias and sky flat-field frames following standard procedures. Point-spread function photometry was performed, and photometry was calibrated relative to Pan-STARRS1 photometric standards (H. A. Flewelling et al. 2020). Similarly, the photometry of the images from the Thacher telescope was obtained using `DoPhot` and calibrated with the *griz* Pan-STARRS1 catalog.

Figure 1 shows our photometric data of SN 2021foa, including LCO/Sinistro (*UBVRI*, *up*, *gp*, *rp*, *ip*, *z*), our re-reduced and host galaxy subtracted UVOT (*UVW*1, *UVW*2, *UVM*2, *U*, *B*, and *V*) data, ATLAS (*c* and *o*), Nickel (*BVri*), and Thacher (*griz*) data. All photometric data are summarized in Table A1.

2.2. Spectroscopic Data

Figure 2 shows our extensive optical spectroscopic follow-up observations of SN 2021foa obtained within −12 days and +427 days. Data were obtained with the Kast dual-beam spectrograph (J. S. Miller & R. P. S. Stone 1993) on the Lick Shane 3 m telescope at −7, +8, +15, +21, +35, +42, and +51 days, the Goodman spectrograph (J. C. Clemens et al. 2004) on the NOIRLab 4.1 m Southern Astrophysical Research (SOAR) telescope at Cerro Pachón at −8 days, the Alhambra Faint Object Spectrograph and Camera (ALFOSC) on the Nordic Optical Telescope (NOT) at −11, −7, and −6 days, and the Wide Field Spectrograph (WiFeS) at the Australian National University (ANU) 2.3 m telescope located at Siding Spring Observatory (M. Dopita et al. 2007) at −11 and +51 days.

The Kast observations are performed with the blue side 452/grism, 300/7500 grating, d58 dichroic, and 2″ slit. Goodman observations were carried out using the 400 lines/mm grating with the M1 wavelength setting (300−705 nm). To reduce the Kast and Goodman spectra, we used the `UCSC_spectral_pipeline`[18] (M. R. Siebert et al. 2019). The ALFOSC spectra were taken with a 1.″0 slit and grisms 4 and 8. For all reduction, extraction, and calibration steps, we used standard `IRAF`[19] routines using `PyRAF`.[20]

WiFeS is an integral-field spectrograph with a field of view of 38″ × 25″. SN 2021foa was observed using an RT-560 beam splitter and B3000 and R3000 diffraction gratings, which cover the 3200–5900 Å and 5300–9800 Å wavelength ranges. All observations had a $Y = 2$ binning readout mode, corresponding to a 1×1 arcsec^2 spaxel. Each observation was reduced using `PyWiFeS` (M. J. Childress et al. 2014). We extract an isolated part of the sky for background determination and subtraction.

Figure 3 presents our NIR spectra of SN 2021foa, which were obtained with the SpeX spectrograph (J. T. Rayner et al. 2003) mounted on the 3 m NASA Infrared Telescope Facility (IRTF) at −8, +12, and +41 days. In this mode with the 0.″8 slit, the spectral resolving power is $R \approx 1000$. The SN was observed in an ABBA dithering pattern with an A0V star observed immediately before or after science observations for telluric correction. We also obtain observations of internal flat field and arc calibration lamps at the science pointing. We reduced the data using `Spextool` (M. C. Cushing et al. 2004), which performed flat-fielding, wavelength calibration, background subtraction, and spectral extraction. We then performed telluric correction using `xtellcor` (W. D. Vacca et al. 2003).

Medium-resolution spectra were obtained with the X-shooter echelle spectrograph (J. Vernet et al. 2011) mounted at the Very Large Telescope (VLT) at the European Southern Observatory (ESO) on Cerro Paranal, Chile. The data are presented in Figures 2 and 3. The X-shooter instrument covers the wavelength range of 0.3–2.5 μm in three arms: the ultraviolet and blue (UVB), visual (VIS), and near-infrared (NIR) wavelength ranges. The slit widths (and resolving power) for the UBV, VIS, and NIR for these observations were 0.″9 ($R = 5900$), 1.″0 ($R = 8900$), and 1.″0 ($R = 5600$), respectively. UVB, VIS, and NIR arms were reduced with `EsoreFlex 2.11.5`[21] (W. Freudling et al. 2013) pipeline individually. Then, using a custom `Python` code, the UVB and VIS arms were combined in `STARE` mode, while the NIR arm was combined in `NOD` mode. Special efforts have been made to perform a detailed background subtraction around strong host galaxy emission lines such as Hα (see Figure A1).

[18] https://github.com/msiebert1/UCSC_spectral_pipeline
[19] https://iraf-community.github.io
[20] https://github.com/iraf-community/pyraf
[21] https://www.eso.org/sci/software/esoreflex/

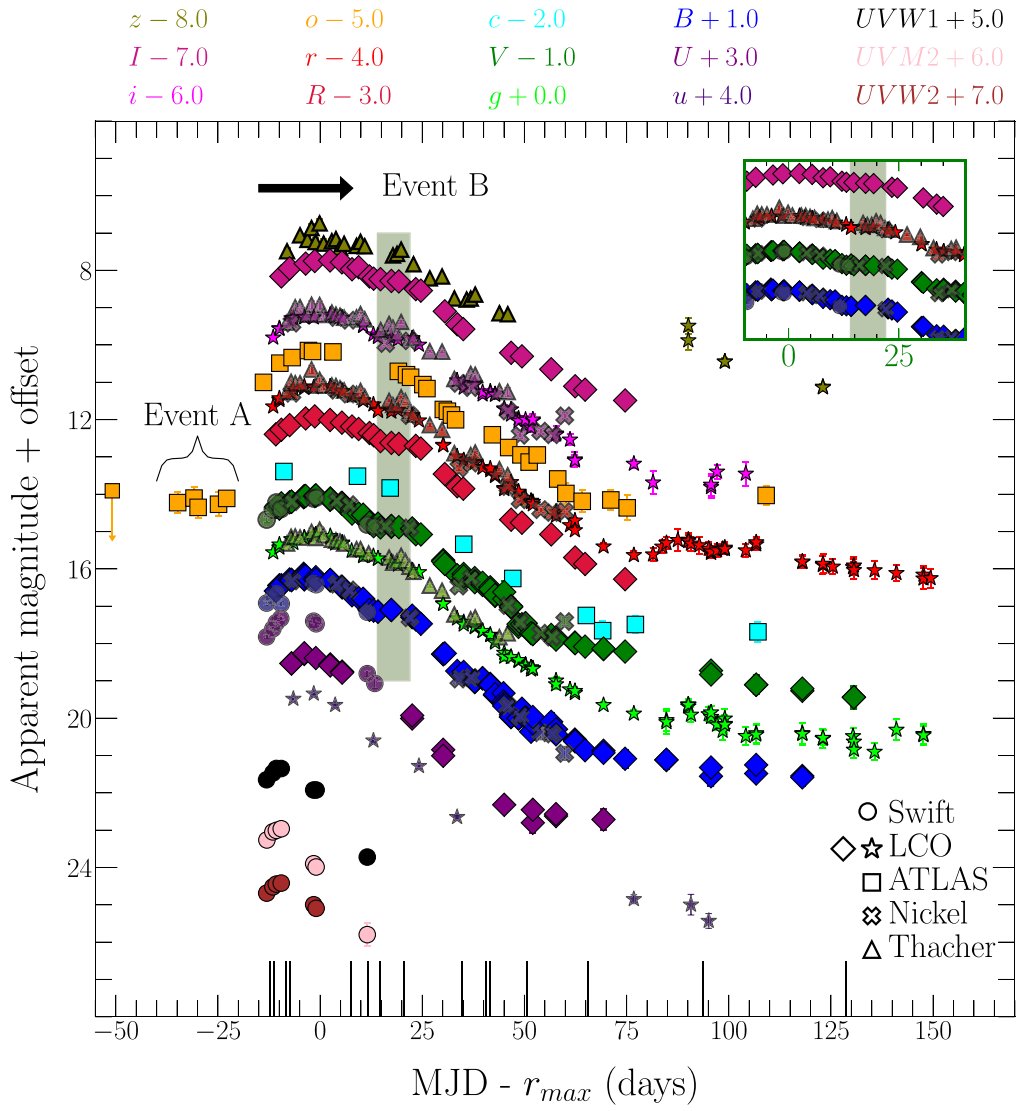

Figure 1. Photometry of SN 2021foa. Swift *UVW1, UVM2, UVW2*, Thacher *griz*, Nickel *BVri*, and LCO/Sinistro *UBVRI*, *up*, *gp*, *rp*, *ip*, *z* data (AB system) are denoted by symbols and color coded as described in the legend. All light curves are offset by a constant, for clarity. The gray vertical lines mark our spectroscopic data at their respective epochs relative to $r_{\rm max}$ at $\rm MJD_{max}$ = 59302.35 days. Event A encompasses the time when the light curve of SN 2021foa shows precursor emission. Uncertainties are smaller than the size of the markers. The green band delimits the phases where a short plateau is observed (from +14 to +22 days). The inset highlights that same phase region.

To improve the flux calibration from the mentioned pipelines, we mangle all low-resolution spectra to the interpolated photometry from `extrabol`,[22] as described in Section 3.1.1. The .9UBV and VIS arms of the first three VLT/X-shooter spectra (+66, +95, and +129 days) were also flux calibrated in this way. Due to the lack of NIR photometry at these epochs, we used the calibration provided by `EsoReflex`. The same approach was applied for the last spectrum at +427 days, and as this late-time spectrum includes minimal contamination from the SN, we use narrow Hα to determine the redshift ($z = 0.0086183$).

2.3. Extinction

The Milky Way extinction was obtained from E. F. Schlafly & D. P. Finkbeiner (2011), i.e., $E_{(B-V)_{\rm MW}}$ = 0.072 for $R_V = 3.1$, and the host galaxy extinction, $E_{(B-V)_{\rm host}}$ = 0.129, was adopted from A. Reguitti et al. (2022). We confirmed this value from measurements of the equivalent width (EW) of the Na ID (λ5890, 5896) absorption lines detected in our medium-resolution VLT/X-shooter spectra (see Section 3.2) together with the extinction–EW relation from M. Turatto et al. (2003). We obtain an EW of 0.85 ± 0.36 Å, similar to measurements by A. Reguitti et al. (2022).

[22] https://github.com/villrv/extrabol

3. Analysis Methodology

The rich photometric and spectroscopic data set shows that SN 2021foa has a prolonged precursor emission similar to the SNe IIn 2009ip, but spectroscopically closer to transitional SNe IIn/Ibn objects, with strong He I emission lines in the optical and NIR wavelengths. To understand the physical mechanism that drives the similarities and differences and to put together a coherent physical scenario that can explain all observables, we employ a range of analysis methods. First, we model the multiband photometry to obtain information about the progenitor and the CSM associated with SN 2021foa, such as the ejecta and CSM masses and

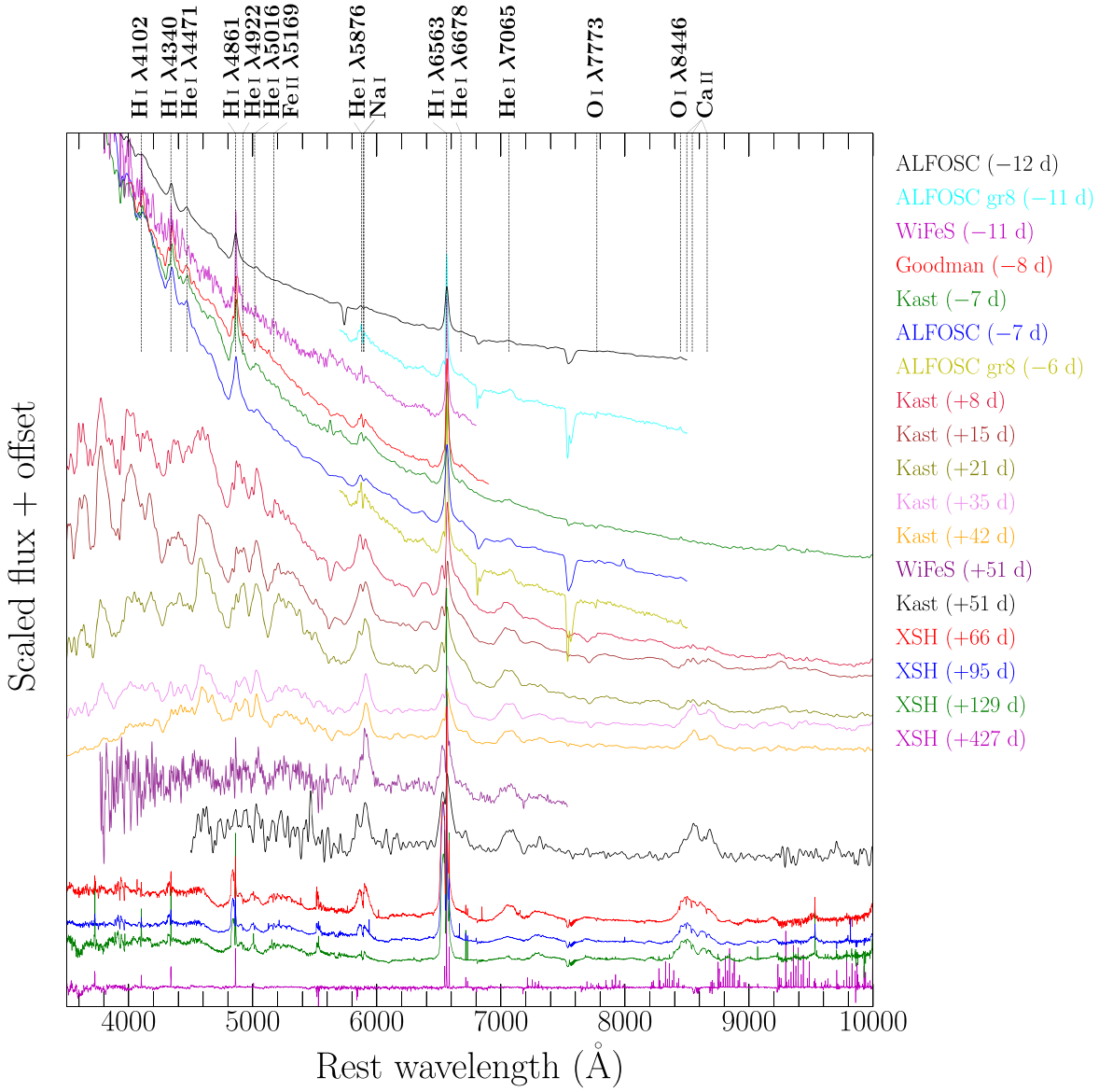

Figure 2. Low and medium (XSH; VLT/X-shooter) resolution optical spectra of SN 2021foa (Section 2.2, Table A2). Black, dashed vertical lines indicate the rest-frame wavelength of the strongest lines observed in SN 2021foa, mostly H I and He I lines. For visualization purposes, we smoothed all the spectra with a rolling Gaussian with a kernel size of ∼15 Å.

(The data used to create this figure are available in the online article.)

progenitor radius. Second, we investigate the evolution of the most prominent lines (e.g., H I, He I, Ca II) of SN 2021foa by fitting their broad and narrow velocity components in emission and absorption. Such analysis provides insights into the complexity of the CSM while also highlighting the transitional nature of SN 2021foa among SNe IIn and Ibn classes. Lastly, we fit two blackbody (BB) functions to the X-shooter spectra from optical to NIR wavelengths to estimate the temperature and amount of dust present at the respective epochs in SN 2021foa.

3.1. Photometry

We begin with an analysis of the photometry of SN 2021foa, including a comparison to well-studied sources to inform the timescales and energetics of the explosion, which in turn constrain the progenitor system. Figure 4 shows the ATLAS *o*-band light curve of SN 2021foa compared to *R*-band-like (*o*, *r*, and *R*) light curves of other interacting SNe. Our comparison sample consists of transitional SNe IIn/Ibn 2005la, 2011hw, iPTF15akq, and 2020bqj. We also include SNe AT2016jbu, 2005gl, and 2016bdu, members of the 2009ip-like class with a photometric resemblance to SN 2021foa. The prototypical SNe Ibn SN 2006jc and SN 2023fyq (ATLAS photometry using `ATClean`, S. Rest et al. 2023) serve as a representation of a well-studied, interacting He-rich SN. Additionally, we compare SN 2021foa against the SNe Ibn template from G. Hosseinzadeh et al. (2017), which represents the average, homogeneous photometric evolution of this SN class as well as the weighted mean ($\pm\sigma$) of the photometry of all stripped-envelope, hydrogen-poor SNe Ibc in M. R. Drout et al. (2011). Interestingly, there is a plateau of ≈1 week duration starting from ≈2 weeks after maximum light in SN 2021foa (see the inset in Figure 1). A similar plateau lasting for about 2 weeks can also be observed for SN 2016jbu (S. J. Brennan et al. 2022b).

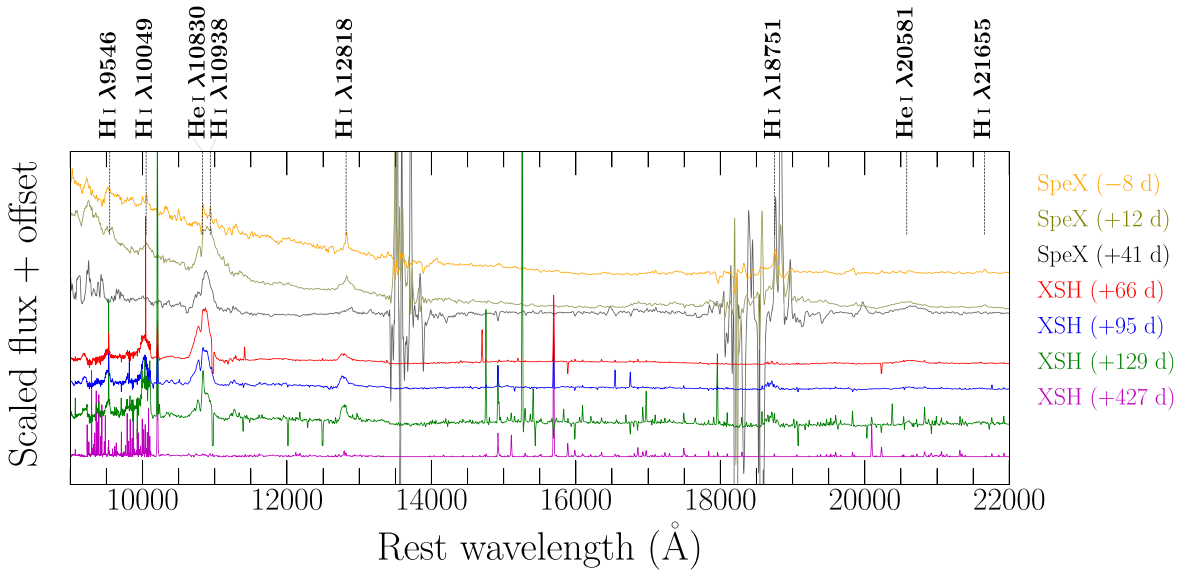

Figure 3. Low and medium (XSH; VLT/X-shooter) resolution NIR spectra of SN 2021foa (see Section 2.2, Table A2). For visualization purposes, the X-shooter spectra were trimmed from 2.2 to 2.5 μm due to low signal-to-noise in that region. All spectra were smoothed with a rolling Gaussian with a kernel size of ∼15 Å. (The data used to create this figure are available in the online article.)

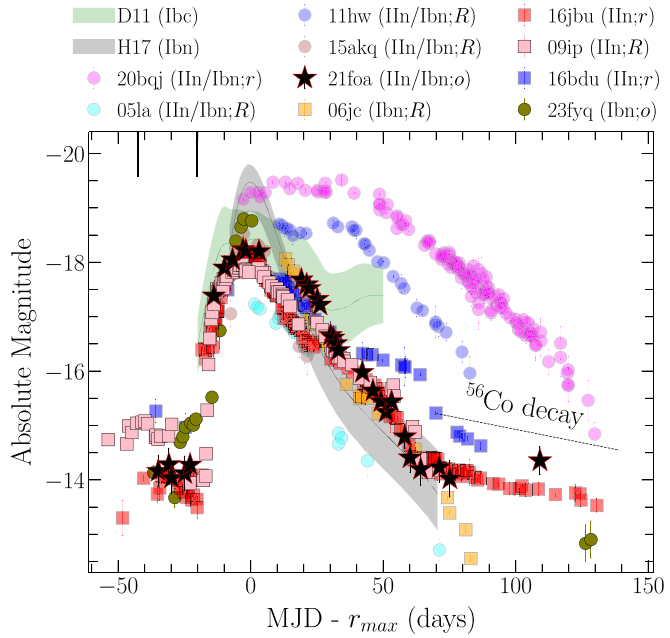

Figure 4. R-/r-band light-curve comparison of interacting SNe IIn/Ibn. Light curves are shown for SNe 2005la (A. Pastorello et al. 2008b), 2011hw (N. Smith et al. 2012a; A. Pastorello et al. 2015a), iPTF15akq (G. Hosseinzadeh et al. 2017), 2020bqj (E. C. Kool et al. 2021), 2021foa (A. Reguitti et al. 2022), 2009ip-like SNe 2009ip (M. Fraser et al. 2013; A. Pastorello et al. 2013), 2016jbu (C. D. Kilpatrick et al. 2018; S. J. Brennan et al. 2022b) and 2016bdu (A. Gal-Yam et al. 2007; A. Pastorello et al. 2018), including the SNe Ibn 2006jc (A. Pastorello et al. 2007) and SN 2023fyq (S. J. Brennan et al. 2024a; Y. Dong et al. 2024). All data are denoted by symbols and color coded according to the legend. The gray-shaded region corresponds to the SNe Ibn template of G. Hosseinzadeh et al. (2017, H17). The green-shaded area is the weighted mean $\pm\sigma$ of the photometric sample of SNe Ibc in M. R. Drout et al. (2011, D11). The reference epoch of SN 2016jbu is with respect to V-band maximum. Vertical lines delimit the event A of SN 2021foa in Figure 1.

SN 2009ip-like SNe are characterized by outbursts of $M_R \sim -11 \pm 2$ mag several years before the explosion, faint emission mimicking SN impostors of $M_R \sim -13 \pm 2$ mag (event A), and a peak magnitude of $M_R \sim -18.5 \pm 0.5$ (event B; A. Pastorello et al. 2018; S. J. Brennan et al. 2022a). For SN 2021foa, we set an upper limit of $M_o \approx -13.4$ mag for any outburst within ∼5 yr before explosion (Section 5.2), while event A ($M_r \approx -14$ mag) and event B ($M_r \approx -18$ mag) agree with the values of 09ip-like class. The peak magnitude of SNe Ibn is, on average, much larger than that of SN 2021foa (M_R = -19.47 $^{-0.32}_{+0.54}$) (G. Hosseinzadeh et al. 2017). Since rise/decay times/slopes depend on the assumed explosion date and the interaction between the CSM and the SN ejecta, it is difficult to quantify the changing behavior of the light curves of 09ip-like SNe. Nonetheless, the decay slopes from +0 to +30 days past r-band maximum of SN 2009ip, AT 2016jbu, and SN 2021foa (∼0.04, ∼0.07, and ∼0.04 mag day^{-1}; D. Farias et al. 2024, in preparation) are smaller than the average decay rate of SN Ibn (0.1 mag day^{-1}; G. Hosseinzadeh et al. 2017). We note that the light curve of SN 2021foa shows a clear rebrightening in the r band after ≈+80 days.

3.1.1. Constructing a Bolometric Light Curve

To obtain the bolometric light curve, we fit the spectral energy distribution (SED) with a BB model using `extrabol` (I. Thornton & V. A. Villar 2022). `Extrabol` models the light curves in flux space as a function of wavelength and phase with a 2D Gaussian process (typically with zero mean and stationary kernels in wavelength and phase, though these are configurable). A model SED (a BB model in the case of SN 2021foa) is fit to match the posterior mean of the Gaussian process, and the resulting SED surface is marginalized over wavelengths to produce a quasi-bolometric light curve. We combined our optical observations in Section 2.1 with J, H- and $griz$-band photometry from A. Reguitti et al. (2022) to construct the SED from the B-band to NIR wavelengths. We computed the bolometric light curve only for epochs for which data were available in all selected passbands, as the 2D Gaussian process regresses to the mean when not constrained by observations.

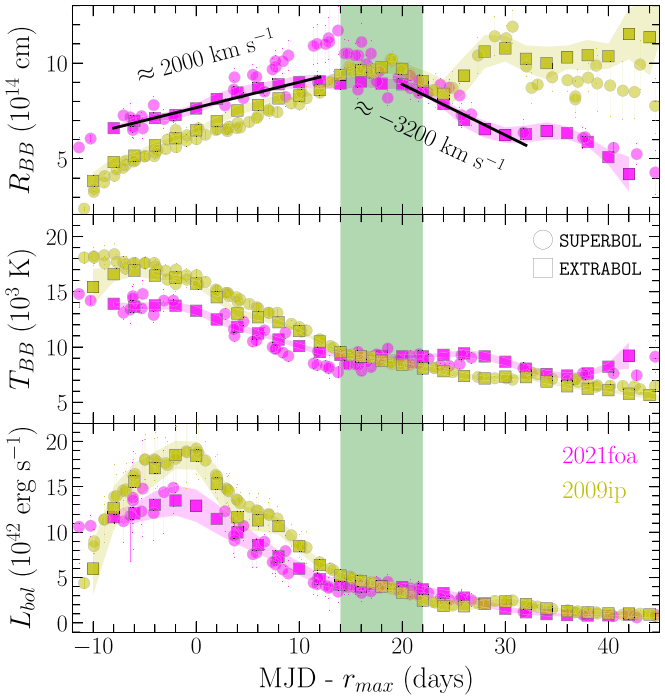

Figure 5. Upper, middle, and bottom panels show the evolution of the radius (R_{BB}), temperature (T_{BB}), and bolometric luminosity (L_{bol}) of SN 2021foa (magenta) and SN 2009ip (yellow) obtained through BB fits to the SED of SN 2021foa using `extrabol` (filled squares) and `SuperBol` (filled circles; M. Nicholl 2018). The green-shaded area represents the epochs of the short plateau in the light curves (see Figure 1).

Figure 5 shows the evolution of the photospheric BB radius (R_{BB}), temperature (T_{BB}), and the resulting bolometric light curve (L_{bol}) using `extrabol`. Additionally, we computed the bolometric light curves using `SuperBol` to show the consistency of our method, assuming a constant color extrapolation at early and late times. For comparison, we also included the bolometric light curve of SN 2009ip, using the *UVW2, UVM2, UVW2, U, B, R, V, I* bands to construct the SED. We address that, even if our fits reproduce the overall evolution of SN 2009ip shown in R. Margutti et al. (2014), they fitted a two-BB function (*hot* and *cold* components) to the SED up to the NIR bands. As expected, the evolution of R_{BB}, T_{BB}, and L_{bol} of both SNe share similarities, such as a monotonic increase of R_{BB} before *r*-band maximum and the phase at which L_{bol} reaches maximum (≈ -2 days). Notoriously, the evolution of R_{BB} drastically changes, possibly due to the inclusion of UV bands to construct the SED of SN 2009ip.

3.1.2. Modeling the Light Curve with the `MOSFiT` Framework

In order to investigate the progenitor properties and its mass-loss history, we adopt the radioactive decay (RD) model of ^{56}Ni + circumstellar interaction (CSI) from the `MOSFiT` (J. Guillochon et al. 2018) framework[23] based on E. Chatzopoulos et al. (2012, 2013). The RD+CSI model has been extensively used to model light curves for different SNe Ibn (E. Karamehmetoglu et al. 2017; E. C. Kool et al. 2021; T. Ben-Ami et al. 2023). `MOSFiT` estimates the posterior probability of a set of parameters from the RD+CSI model given the photometric data and physically informed priors.

[23] https://mosfit.readthedocs.io/en/latest/

3.1.3. Parameterization of the RD+CSI Model

The RD model accounts for the RD of ^{56}Ni through three parameters: the nickel fraction, f_{Ni}, the γ-rays' opacity of the ejecta, κ_γ, and an optical opacity, κ. Additionally, `MOSFiT` includes a model for the SN ejecta–CSM interaction, with several physical quantities for the ejecta and the CSM listed as free parameters (see V. A. Villar et al. 2017 for a detailed description). This includes the total mass of the ejecta (M_{ej}) and the inner and outer density profiles of the ejecta ($\rho_{in,ej} \propto r^{-\delta}$, $\rho_{out,ej} \propto r^{-n}$). The main parameters to describe the CSM are the inner radius of the CSM (R_0), the CSM density (ρ_{CSM}), and the density profile of the CSM ($\rho_{CSM} \propto r^{-s}$). For the latter, $s = 0$ corresponds to a constant density (shell-like) CSM, while $s = 2$ denotes a wind-like model. Additionally, `MOSFiT` fits for the explosion time (t_{exp}) relative to the first photometric observation (E. C. Kool et al. 2021). `MOSFiT` also includes some nuisance parameters, such as the minimum allowed temperature of the photosphere before it recedes, T_{min}. Finally, a white noise term, σ, is included and added in quadrature to the photometric uncertainties. `MOSFiT` uses this white noise term to quantify the quality of the fitting. Acceptable values for this parameter are $\sigma < 0.2$ (M. Nicholl et al. 2017).

3.1.4. RD+CSI Modeling Choices and Priors

While this is a high-dimensional model, the fundamental physical parameters of interest to this study are f_{Ni}, M_{ej}, M_{CSM}, E_{kin}, and R_0. We fix three parameters of the model: $\delta = 1$, $n = 12$, and s. The assumed value of $n = 12$ is typically used to characterize RSG-like progenitors rather than for BSG/W-R stars, but δ and n are not sensitive to derive the fundamental parameters (V. A. Villar et al. 2017; E. C. Kool et al. 2021). In order to investigate shell- and wind-like CSM configurations, we fixed $s = 0$ and $s = 2$, respectively. With these choices, 11 free parameters remain: f_{Ni}, κ, M_{ej}, M_{CSM}, ρ_{CSM}, R_0, E_{kin}, t_{exp} (i.e., fundamental parameters) and T_{min}, κ_γ, and σ (the nuisance parameters). To constrain the explosion time of SN 2021foa, we only considered observations from -20 days onward, i.e., we discarded event A photometry as the RD+CSM model was not designed to model precursor emission. We used top-hat priors on the remaining parameters. We note that other physical parameters, including κ_γ, κ, and t_{exp} may be considered nuisance parameters as these are quantities that are not observable. These physically informed modeling choices and priors significantly reduce the dimensionality of the problem and help ensure that the inferred quantities are meaningful.

Following E. C. Kool et al. (2021), we elected to use the dynamic nested sampling implemented in `DYNESTY` (J. S. Speagle 2020). Nested samplers estimate the evidence ( ), i.e., the marginalized likelihood for the data given the model. Given that our prior distributions are constant for $s = 0$ and $s = 2$, we can directly compare the evidence reported by `DYNESTY` to check which model is preferred given our data (i.e., the model with larger evidence).

In order to reduce the computational cost without oversampling the observations per epoch, we provided `MOSFiT` with the following bands: *UVW2*, *UVM2*, *UVW1*, *U*, *B*, *V* (UVOT), *u*, *B*, *g*, *V*, *r*, *i*, *z* (A. Reguitti et al. 2022), *o*, *c* (ATLAS) and *up*, *gp*, *rp*, *ip* (LCO). Figure 6 shows the `MOSFiT` model light curves for $s = 0$ and $s = 2$ for a collection of bands considered, together with the observed data. The parameters of the model are summarized in Table 1 and discussed in Section 4.2.

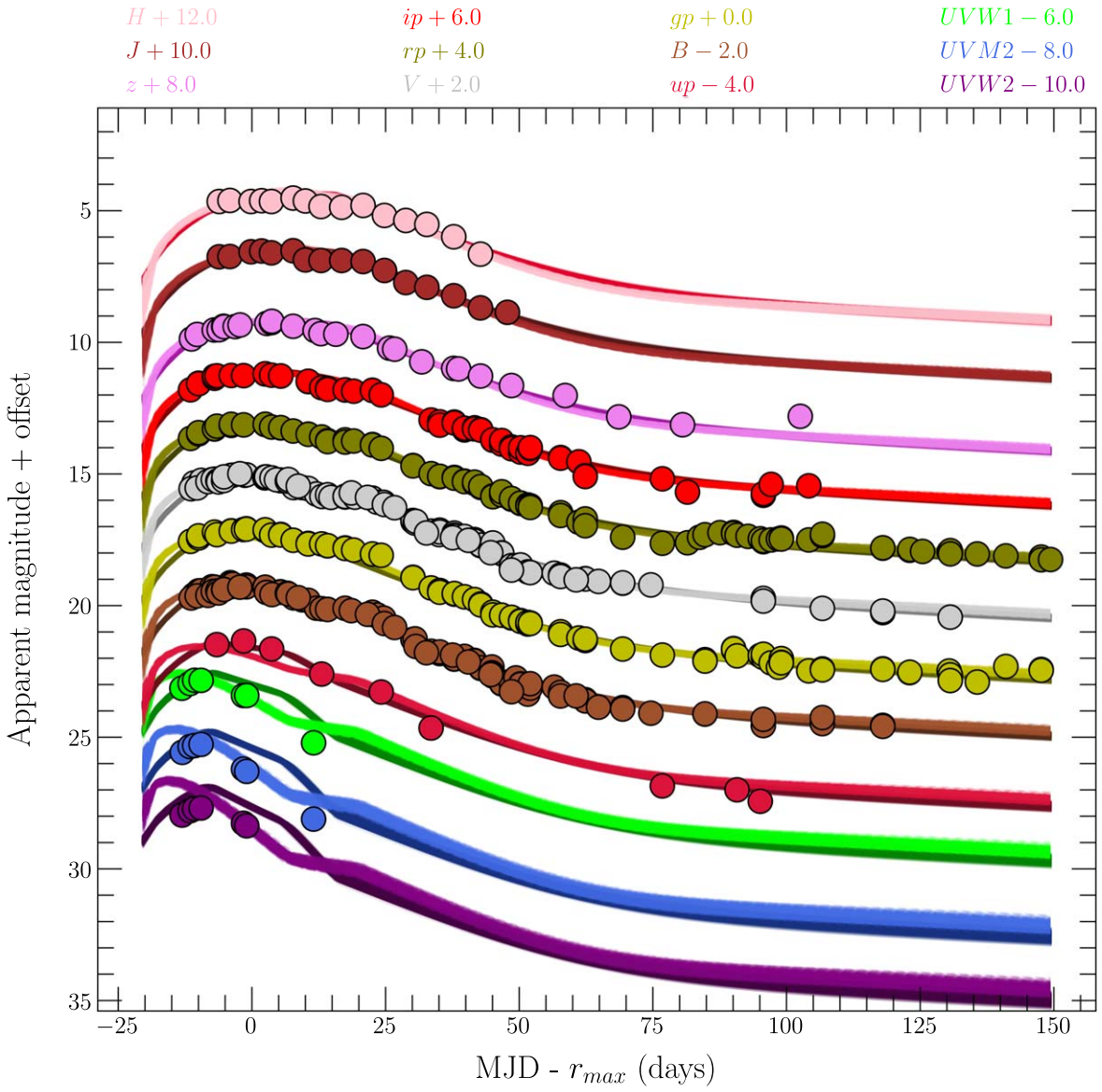

Figure 6. Collection of light curves of SN 2021foa in several bands reported in this work and A. Reguitti et al. (2022). Color symbols are the photometric data. Light and bold color lines are 1000 sampled MOSFiT light curves from the posterior distribution for the shell ($s = 0$) and wind-like CSM configuration ($s = 2$), respectively.

3.2. Spectroscopy

Our multi-epoch spectroscopy permits a detailed analysis of the evolution of the prominent emission and absorption line profiles of SN 2021foa (see Figures 2 and 3) over a large range of epochs. We select the spectra with the highest resolution, including those published by A. Reguitti et al. (2022) at +35, +43 days. For simplicity, we refer to any "velocity component" of a line profile as "component."

3.2.1. Spectral Line Fitting

In order to quantify the evolution of the different components of the Balmer lines (Hα, Hβ, Hγ, and Hδ, panels (A), (B), (C), and (D) in Figure A3), we fit the lines with multiple Gaussian and Lorentzian functions (see Figure 7). Prior to this, we fit the continuum in the respective wavelength region of the emission lines (around $\pm$5000 km s^{-1}) using a 1D polynomial and subtract it. Furthermore, to account for either low instrumental resolution or a low signal-to-noise ratio (SNR), we convolved the spectral region of the emission lines with a Gaussian kernel that has a standard deviation $\leqslant 2\times$ the dispersion (approximate resolution) of the instrument (see Table A2). We detail the line profile fitting method for Hα as an example.

For the first two epochs (-11 and -8 days), we simultaneously fit the complex Hα emission line with two functions. Since the Hα exhibits broad wings, we fit a Lorentzian profile to the broad base of the emission line and a Gaussian profile to the narrow component. The introduction of the Lorentzian profile was made to account for any electron scattering wings at early times (C. Fransson et al. 2014). For all epochs between -3 and +51 days, we fit the Hα emission line with three Gaussian functions, one each for the narrow absorption, narrow emission as well as for the broad emission profile. At all late epochs (+66 to +129 days), we add another Gaussian profile to fit the strongly blueshifted emission of Hα. For all other H I emission lines, we follow a similar method with two minor differences: (i) the central wavelength used to extract the line profile and (ii) the number of Gaussian functions to fit the line profiles. For example, for Paβ, a single Gaussian profile can

Table 1
Fundamental Parameters of the Shell-like ($s = 0$) and Wind-like ($s = 2$) MOSFiT (CSM-Ni) Models

Parameter[a]	Units	Prior	Model	
			$s = 0$	$s = 2$
f_{Ni}	10^{-2}	10^{-3}–1.0	$7.85^{+0.41}_{-0.38}$	$1.85^{+0.09}_{-0.09}$
κ	cm^2 g^{-1}	0.1–0.4	$0.396^{+0.003}_{-0.006}$	$0.34^{+0.037}_{-0.043}$
E_{kin}	10^{51} erg	0.01–20	$0.2^{+0.01}_{-0.01}$	$1.79^{+0.07}_{-0.06}$
M_{CSM}	$M_\odot$	0.01–30.0	$0.39^{+0.01}_{-0.01}$	$0.07^{+0.01}_{-0.01}$
M_{ej}	$M_\odot$	1.0–30.0	$1.91^{+0.08}_{-0.08}$	$8.35^{+0.4}_{-0.4}$
R_0	10^{14} cm	0.02–20.0	$0.15^{+0.58}_{-0.11}$	$0.7^{+0.14}_{-0.13}$
ρ_{CSM}	10^{-12} g cm^{-3}	10^{-3}–10^4	$0.65^{+0.03}_{-0.02}$	$52.86^{+28.86}_{-15.76}$
t_0	Days	−30–−20	$-25.3^{+0.07}_{-0.04}$	$-21.45^{+0.15}_{-0.17}$
σ	Mag	10^{-5}–10	$0.199^{+0.006}_{-0.005}$	$0.193^{+0.005}_{-0.005}$
M_{Ni}	$10^{-2}M_\odot$	⋯	$1.5^{+0.1}_{-0.1}$	$1.54^{+0.11}_{-0.1}$
v_{ej}	10^3 km s^{-1}	⋯	$4.15^{+0.12}_{-0.12}$	$5.98^{+0.19}_{-0.17}$
log	⋯	⋯	789.8 ± 0.2	817.3 ± 0.2

Note.
[a] Parameters of the RD+CSI model are the nickel fraction (f_{Ni}), optical opacity (κ), kinetic energy (E_{kin}), ejecta mass (M_{ej}), CSM inner radius (R_0), CSM density (ρ_{CSM}), explosion epoch with respect to r_{max} (t_0), nickel mass (M_{Ni}), ejecta velocity (v_{ej}), and the evidence, (log), detailed in Section 3.1.4.

well fit the emission line that neither exhibits narrow emission nor absorption.

For the He I lines, we only quantify the evolution of the strongest emission lines in the optical (He I λ5876 and 7065). We fit these symmetric features with a single Gaussian at all epochs (see Appendix C.4). This is the simplest model that is consistent with the observations.

We also identify narrow absorption lines of Fe II λλ5169, 5276, 5317, (likely) He I λλ4922, 5016, Ca II λλ8498, 8542, 8662, and O I λ8446 (see Figures A3 and A4). To quantify the velocity evolution of the region harboring these elements, we fit a single Gaussian profile to the absorption lines.

Finally, we calculate the total line flux of all H I emission lines from the continuum-subtracted line profile fits. We exclude the emission lines from the host galaxy at late epochs (>+40 days). The total emission line flux of the He I λ5876 line complex is estimated from the continuum-subtracted data directly. The emission line complex is in the velocity range of ±6000 km s^{-1}.

3.3. Modeling the Late-time VLT/X-shooter Spectra

A signature of either preexisting or newly formed dust is the thermal (near) infrared excess emission of hot dust grains over the SN continuum emission. Such thermal emission has been observed in several types of CCSNe (see C. Gall et al. 2011, for a review). To test if dust is present in SN 2021foa, we fit the continuum emission from optical to the NIR wavelengths of our late-time SN 2021foa VLT/X-shooter spectra at +66, +95, and +129 days. We exclude the spectral regions containing strong emission lines such as Hα and the He I λ10830 + and Paγ complexes prior to fitting as indicated in Figure 8.

We then simultaneously fit a BB function to the hot SN photosphere and a modified blackbody (MBB) function (R. H. Hildebrand 1983) to the NIR excess emission to account for any hot dust emission as

$$F_\lambda(\lambda) = \frac{R_{SN}^2}{D_L^2} B_\lambda(\lambda, T_{SN}) + \frac{M_d}{D_L^2} \kappa_{abs}(\lambda, d) B_\lambda(\lambda, T_d), \quad (1)$$

with D_L the luminosity distance to the SN, R_{SN} the radius of the photosphere, and $B_\lambda(\lambda, T)$ the Planck function at temperatures of the photosphere, $T = T_{SN}$ and dust, $T = T_d$. We assume optically thin dust, with a dust mass M_d, which is distributed spherically symmetrically around the SN. For the dust mass absorption coefficient, $\kappa_{abs}(\lambda)$, we adopt the formalism of C. Gall et al. (2017), where $\kappa_{abs}(\lambda)$ follows a $\lambda^{-\beta}$ power law in the VLT/X-shooter NIR wavelength range. Thus, $\kappa_{abs}(\lambda)$ can be parameterized as $A_d(\lambda/1\,\mu m)^{-\beta}$, with $A_d = 1.0 \times 10^4$ cm^2 g^{-1} and $\beta = 1.5$. This formalism mimics small-sized ($\lesssim$0.1 μm) carbonaceous grains (e.g., F. Rouleau & P. G. Martin 1991).

4. Analysis Results

4.1. Estimating Photosphere Expansion Velocity from the Bolometric Light Curve

The evolution of T_{BB} follows the bolometric light curve. The peak values of L_{bol} and T_{BB}, reached between −5 and 0 days, are $\approx 1.7 \times 10^{43}$ erg s^{-1} and ≈15,000 K, respectively. The temperature evolution flattens between 14 and 23 days, as indicated by the green-shaded region in Figure 5. This coincides with the short light-curve plateau that is observable in several optical passbands (see Figure 1 and Section 3.1). Subsequently, T_{BB} decreases to 8000 K at day +35. On the other hand, R_{BB} is largest, with about 10^{15} cm at the beginning of the short light-curve plateau.

From the estimated slope of the R_{BB} evolution until this maximum at ∼+10 days, we infer an expansion velocity of the photosphere of ≈2000 km s^{-1}. Thereafter, R_{BB} recedes at a velocity of ∼−3200 km s^{-1} to a radius of $\approx 6 \times 10^{14}$ cm at day ∼+30, the same level as at −10 days.

4.2. Estimating Progenitor Properties from the RD+CSI Model

We use the parameters of the RD+CSI model inferred with the MOSFiT framework (Section 3.1.2, Table 1) to constrain progenitor and SN properties. From the evidence values (log), $s = 2$ model is preferred over $s = 0$. We obtain an ejecta mass of $\approx 2.0\,M_\odot$ for a $s = 0$ (CSM-shell-like) model. This value is close to the maximum mass of $\approx 1.2\,M_\odot$, as estimated for any progenitor (single or in a binary system) of SNe Ibn (L. Dessart et al. 2022). However, the ejecta mass inferred for $s = 2$ is $\approx 8\,M_\odot$. This is lower than the average value of $\approx 16\,M_\odot$, as obtained for SNe Ibn SN 2019uo (A. Gangopadhyay et al. 2020), 2020bqj (E. C. Kool et al. 2021), and PS15dpn (S.-Q. Wang & L. Li 2020).

The CSM mass is ∼0.4 and ∼0.1 $M_\odot$ for the $s = 0$ and $s = 2$ models, respectively. This is consistent with the CSM mass estimates of 0.016 $M_\odot$ and <0.1 $M_\odot$ for SN 2016jbu (S. J. Brennan et al. 2022a; 0.016 $M_\odot$) and typical SNe Ibn (K. Maeda & T. J. Moriya 2022), respectively.

The resulting CSM inner radius, R_0, and the CSM density ρ_{CSM} for the $s = 0$ model are $\sim 2 \times 10^{13}$ cm and $\sim 6 \times 10^{-13}$ g cm^{-3}. For the $s = 2$ model, $R_0 \sim 7 \times 10^{13}$ cm and $\rho_{CSM} \sim 5 \times 10^{-11}$ g cm^{-3}.

Following the E. Chatzopoulos et al. (2012) approach, we can derive the value of R_f, the outer radius of the CSM. For the

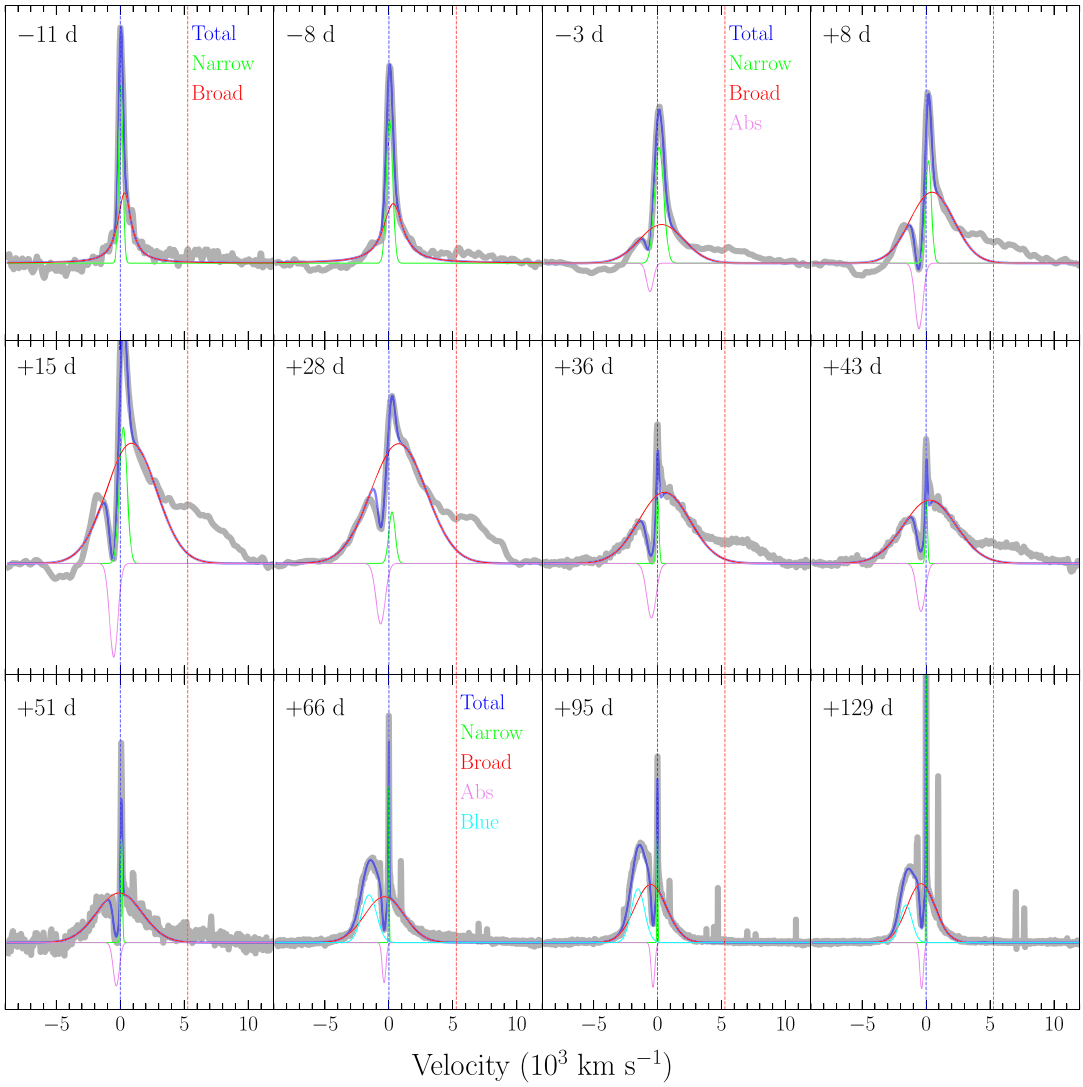

Figure 7. Modeling of the Hα profiles. Zero velocity corresponds to the rest wavelength of Hα line. The first two epochs were fitted using a combination of a Gaussian and Lorentzian profile (red, green), while the spectra from −3 to +51 days are fit by three Gaussians, accounting for the narrow and broader emission (green and red), and the absorption (purple). For the medium-resolution spectra (+66, +95, and +129 days), an additional Gaussian component has been added to fit the profile (turquoise). Blue- and red-dashed vertical lines mark the velocities of the rest-frame wavelength of Hα and He I 6678 Å, respectively.

preferred model ($s = 2$), $R_f \approx 1.5 \times 10^{14}$ cm, while for $s = 0$, $R_f \approx 7 \times 10^{14}$ cm.

While the MOSFiT framework is flexible, the fundamental parameters of the RD+CSI model are not always directly expressed as standard literature quantities, such as nickel mass and mass-loss rate. For the $s = 2$ model, we can estimate the mass-loss rate, M, using the formalism of T. Ben-Ami et al. (2023) and E. C. Kool et al. (2021) as

$$M(r) = 4\pi \rho_{\rm CSM} r^2 v_w, \quad (2)$$

where v_w is a steady CSM wind velocity. Additionally, for the $s = 0$ and $s = 2$ models, we calculate the nickel mass as $M_{\rm Ni} = M_{\rm ej} \times f_{\rm Ni}$ and ejecta velocity $v_{\rm ej} = \sqrt{\frac{10}{3}\frac{E_{\rm kin}}{M_{\rm ej}}}$.

Using Equation (2) to estimate a mass-loss rate, and assuming a wind velocity, $v_w \sim 400$ km s^{-1} as inferred from the velocity of the absorption minima of the H I lines at late times, together with values of R_0 and $\rho_{\rm CSM}$ as resulting from the $s = 2$ model we obtain a mass-loss rate $\sim 2\,M_\odot$ yr^{-1}. This mass-loss rate is not expected for typical LBV and W-R winds (N. Smith 2017, $\sim 10^{-4}$–$10^{-5}\,M_\odot$ yr^{-1}), but has also been estimated for the SNe IIn iPTF13z (A. Nyholm et al. 2017), 2017hcc (N. Smith & J. E. Andrews 2020), and the SNe Ibn SN 2019kbj (T. Ben-Ami et al. 2023). From X-ray observations, the mass-loss rates of SN 2009ip and 09ip-like SN 2010mc are estimated below $10^{-1}\,M_\odot$ yr^{-1} (E. O. Ofek et al. 2013a, 2013b; I. Boian & J. H. Groh 2018), while the SNe Ibn SN 2022ablq has an upper limit of $0.5\,M_\odot$ yr^{-1} (C. Pellegrino et al. 2024).

4.3. Determining CSM Structure from the Line Evolution

Figure 9 presents the evolution of the full width at half-maximum (FWHM) of the strongest H I lines, inferred from the spectral modeling described in Section 3.2.1 and summarized in Table A3. For the first +40 days, the FWHM of the broad and the absorption components remain constant at about 4000 km s^{-1} and 800 km s^{-1}, respectively.

Between +40 and +60 days, the FWHM of all absorption components decreases by ∼50%, remaining constant at this level until about 130 days. This suggests a second structural

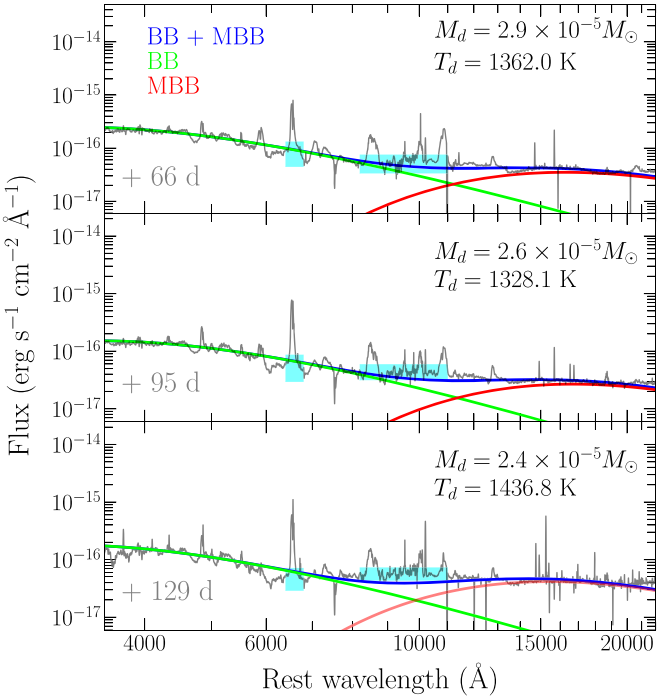

Figure 8. SN and dust fit to VLT/X-shooter spectra at +66 days (upper panel), +95 days (middle panel), and +129 days (lower panel). The SN hot BB function (green curves—dominant below ≈8000 Å) is fit simultaneously with an MBB function to describe the NIR dust emission (red curves) to the observed spectra (black). The blue curves show the sum of the two individual components. Filled cyan rectangles illustrate the spectral regions excluded for the fit due to the large number of emission lines.

component in the CSM. The FWHM of the narrow emission component of Hα and Hβ is about 600 km s^{-1} during the first 20 days. Thereafter, it rapidly declines to about 60 km s^{-1} at which it remains constant from +66 days onward.

Figure 10 shows the evolution of the velocity of the absorption minima of He I, Ca II, O I, and Fe II, and Hβ, summarized in Table A4. It is evident that the velocities of the He I, Ca II, O I, and Fe II absorption lines are at velocities that are $\gtrsim$200 km s^{-1} lower than Hβ. The spectra exhibit a sudden decline of the narrow absorption velocities to about 100 km s^{-1} past +60 days for all transitions (see Figures 9 and 10).

4.3.1. Line Fluxes and Ratios and the Curious Case of SN 2021foa's "Flip-flop"

Figure 11 shows the evolution of the calculated emission line fluxes of the strongest H I and He I lines (summarized in Table A5). The line fluxes of H I including Paβ and He I evolve in a similar fashion up to +50 days. They increase up to +12 days after which they stay constant until about +22 days. This agrees with the plateau phase of the *r*- and *g*-band light curves, as shown for comparison in the upper panel of Figure 11. At later epochs (> + 60 days), all He I and Hδ line fluxes decrease, while most H line fluxes remain constant (or increase, as evident with Hα). Interestingly, at these same epochs, the decline in the *r* band halts (see Figure 1). We find that the He I λ5876 and Hα lines reach approximately the same line flux of 10^{-13} erg s^{-1} cm^{-2} around +20 days, consistent with the findings of A. Gangopadhyay et al. (2024). This is in contrast to A. Reguitti et al. (2022), who estimate that the He I λ5876 flux is about half of that of Hα at this epoch (see Figure A6).

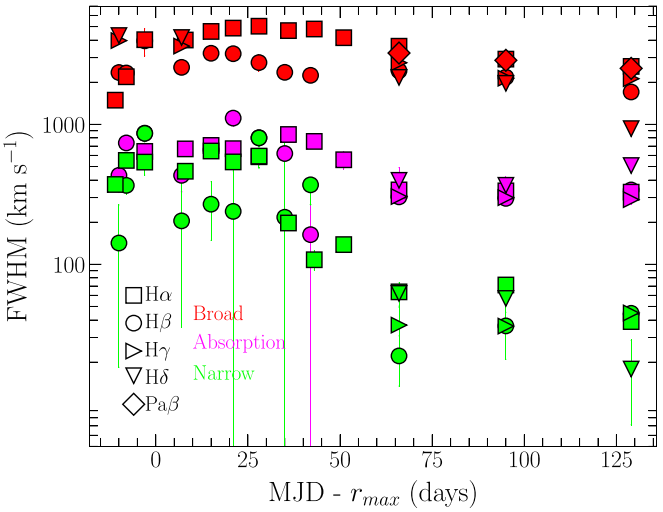

Figure 9. Evolution of the FWHM of H I lines. The broad and narrow emission and the absorption components are color coded (red, green, and magenta). The values of the FWHM are corrected for the resolution of the instrument. If the line was unresolved, an upper limit of the FWHM is estimated as the resolution of the instrument.

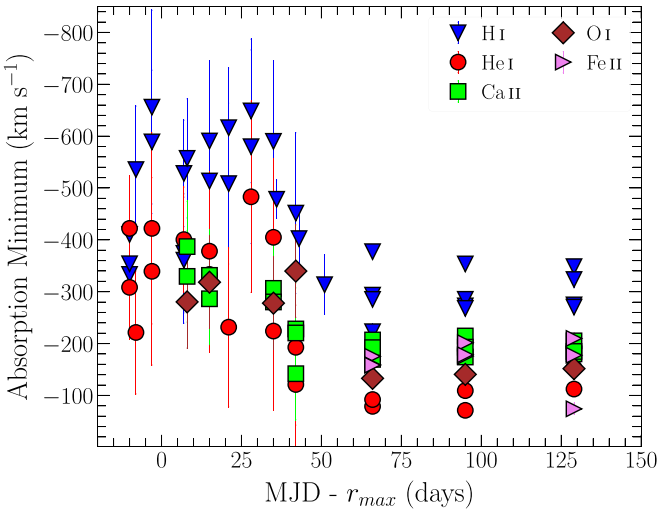

Figure 10. Evolution of the velocity of the absorption minima of H I (Hα, Hβ, Hγ, and Hδ), He I ($\lambda\lambda$4922, 5016), Ca II ($\lambda\lambda$8498, 8542, 8662), Fe II ($\lambda\lambda$5169, 5276, 5317), and O I λ8446 lines.

The flux of He I λ7065 is as strong as that of Hβ for most of the epochs. Figure 12 shows the evolution of the Hα/He I λ5876 line ratio for SN 2021foa in comparison to other transitional SNe IIn/Ibn. These include SNe 2005la, 2011hw, 2020bqj and iPTF15akq. We also include the Hα/He I ratio for the SNe Ibn prototype SN 2006jc and the SNe IIn 2009ip, 2010jl, and 2016jbu. For consistency, we recomputed the line ratios for these objects similar to those of SN 2021foa (see Section 3.2.1). We find discrepancies in the line ratios of SN 2006jc and SN 2011hw of a factor of 2 between N. Smith et al. (2012a) and our measurements (see Appendix C.8). We describe our method to determine the line ratios in Appendix C.9, and attribute this discrepancy to the misestimation of the local continuum surrounding Hα and He I λ5876 lines in previous work.

As shown in Figure 12, all transitional SNe IIn/Ibn have H/He ratios larger than ≈1 at early epochs (< + 10 days).

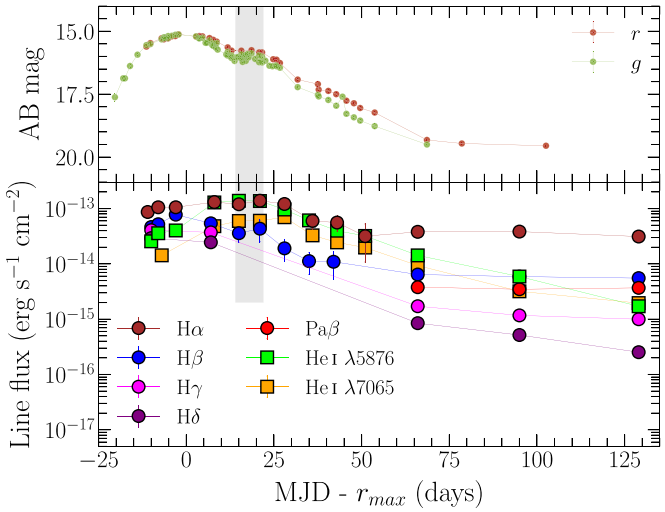

Figure 11. Upper panel: light curves of the g and r bands. Lower panel: evolution of the total emission flux of H I and He I lines. The shaded region encompasses the epochs of the short photometric plateau at ≈+15 days.

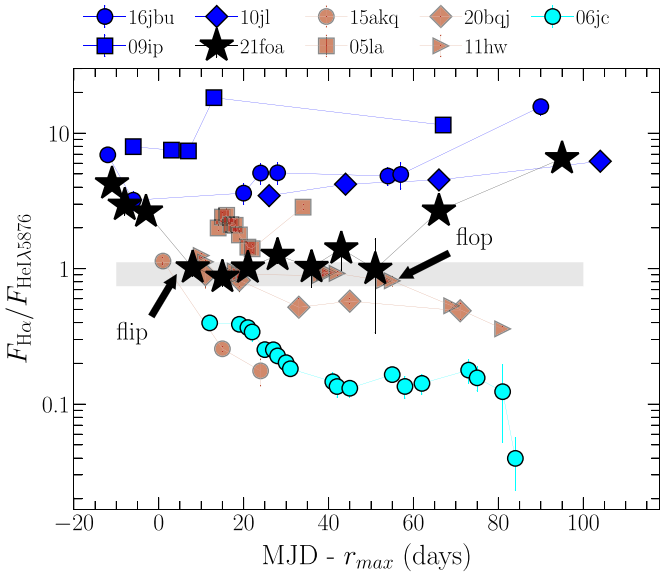

Figure 12. Flux ratio of Hα/He I λ5876 for the transitional SNe IIn/Ibn objects, the SNe Ibn 2006jc and the SNe IIn 2016jbu, 2009ip, and 2010jl. Each class is color coded in red (SNe IIn/Ibn), cyan (SNe Ibn), and blue (SNe IIn). The gray band encompasses the mean and one standard deviation of the line flux ratios of SNe 2011hw, 2020bqj, and 2021foa within +10 to +55 days. Fluxes are averaged in a 3-day bin.

Thereafter, these SNe transit into a more He prominent regime (the "flip"), with a mean Hα/He I ratio of 0.93 ± 0.19 up to about 50 days past peak brightness. After day 50, the line flux ratio of all other transitional SNe IIn/Ibn drops below 1. The evolution of the Hα/He I λ5876 ratio for the transitional SNe IIn/Ibn is clearly different from the classical SNe IIn and 09ip-like events (blue markers), as well as Ibn events such as SN 2006jc (cyan markers). SNe IIn 2016jbu, 2009ip, and 2010jl are hydrogen dominated (Hα/He I > 1) at all epochs. For the Ibn SN 2006jc, the line emission of He I λ5876 dominates at all epochs. It is the presence of a "flip" from hydrogen dominated to a line ratio of ≈1 that truly determines if an object is a member of the class of transitional SNe IIn/Ibn.

However, uniquely for SN 2021foa, even among transitional SNe IIn/Ibn,[24] the line ratio *flips back* (the "flop") to hydrogen dominated after the end of the plateau of the line flux ratio (day +50), and following the rebrightening of H line emission. This double transition "flip-flop" behavior highlights the diversity of these transitional SNe, which ultimately arises from the varied mass-loss histories of their massive star progenitors. We discuss the implications of this observation in Section 5.

4.4. Constraining the Photosphere and Dust Emission Properties from the Late-time VLT/X-shooter Spectra

The fits of the SN 2021foa VLT/X-shooter spectra at +66, +95, and +129 days (see Section 3.3) constrain the radius and temperature of the photosphere, as well as the mass and temperature of the dust. These results are presented in Table 2.

We infer the radius of the SN photosphere at +66 and +95 days of $\approx 2.0 \times 10^{14}$ cm and the temperature ≈9000 K. We can compare this to the inferred R_{BB} and T_{BB} (Section 3.1.1) at the last epoch, ≈+35 days, of our `extrabol` light-curve modeling. The `extrabol` results predict that R_{BB} and T_{BB} decline with time (see Figure 5), and our inferred radius is within the bounds of a linear extrapolation of the `extrabol` prediction at +35 days. We stress that we do not use any `extrabol` extrapolation to constrain the late-time photosphere properties. As such, a linear extrapolation from +35 days to +66 and +95, while the simplest possible model, is likely unphysical. Indeed, the large inferred photospheric temperature from the VLT/X-shooter spectra indicates a shallower evolution.

[24] SN 2005la also shows the *flop*, although the Hα line at ≈ +30 days is overestimated (see Appendix C.9).

Table 2
Fitted Parameters for the BB+MBB Model to the VLT/X-shooter Spectra

Epoch	R_{SN} (10^{14} cm)	T_{SN} (10^3 K)	M_d ($10^{-5} M_\odot$)	T_d (10^3 K)
+66	1.95(01)	9.14(03)	2.88(03)	1.36(002)
+95	1.83(01)	8.47(02)	2.59(02)	1.33(002)
+129	1.49(01)	9.54(06)	2.40(04)	1.44(004)

Note. Fitting uncertainties are given in 10^{-1} units of each column.

At all epochs, the dust mass and temperature inferred for SN 2021foa are $\approx 3 \times 10^{-5} M_\odot$ for a carbonaceous dust composition and ≈1400 K, respectively. However, the inferred low dust temperature indicates that a silicate dust composition can be possible. Adopting a silicate dust composition ($A_d = 0.2 \times 10^4$ cm^2 g^{-1}), the inferred dust mass increases by about a factor of 5 at similar dust temperatures.

5. Interpreting the Observations and Analysis Results

As with all members of the transitional SNe IIn/Ibn, SN 2021foa exhibits characteristics of both SNe IIn and Ibn, albeit with key differences to both classes. SN 2021foa exhibits a short (∼10 days) plateau in the optical light curves about 2 weeks past peak. However, the plateau length is shorter than that of other transitional SNe, such as SN 2011hw and SN 2020bqj (∼50 days, E. C. Kool et al. 2021). Similarly, while there are clear similarities between the spectra of SN 2021foa and SNe Ibn after +22 days, neither SN 2021foa nor any other transitional SNe IIn/Ibn follow the SNe Ibn template of the R-band light curve.

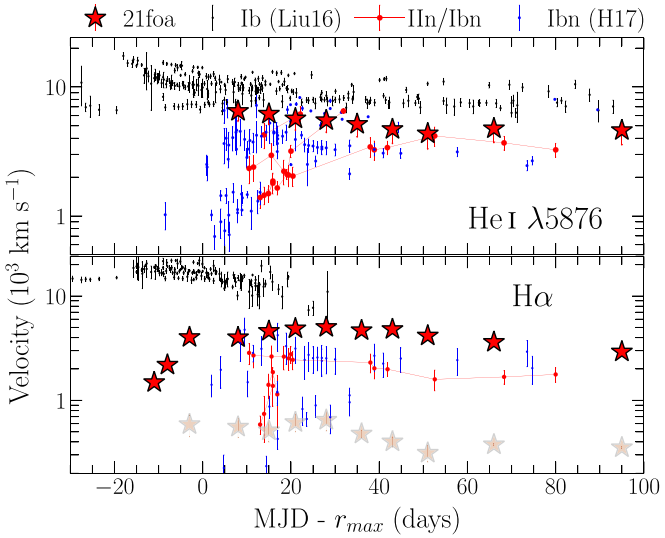

Figure 13. Upper panel: evolution of the velocity of the He I λ5876 for SNe Ib (Y.-Q. Liu et al. 2016, Liu16) and SNe Ibn and SNe IIn/Ibn (G. Hosseinzadeh et al. 2017, H17). Lower panel: same as upper panel, showing the evolution of the velocity of Hα broad (bold) and narrow absorption (light) components.

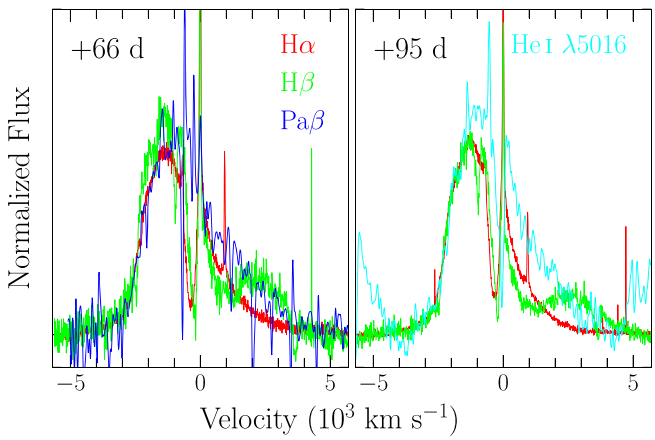

Figure 14. Left panel: normalized VLT/X-shooter spectra of Hα, Hβ, and Paβ at $v \approx -1800$ km s^{-1} (day +66). Right panel: normalized VLT/X-shooter spectra (+95) at $v \approx -1800$ km s^{-1}, comparing Hα, Hβ, and He I λ5016.

However, two aspects make SN 2021foa unique:

1. SN 2021foa is the first clear example of transitional SNe IIn/Ibn that transitions back—a "flip-flop."
2. SN 2021foa exhibited prominent precursor emission about 50–20 days before peak brightness, as is common for SN 2009ip-like objects (Figure 4).

The photometric resemblance of SN 2021foa with 2009ip-like transients may point to a common progenitor system, as already suggested by A. Reguitti et al. (2022). However, the mechanism of producing the precursor emission and the light-curve plateau for SN 2021foa is likely different.

Our spectroscopic analysis of SN 2021foa shows that prominent He I λλ5876, 7065 and Ca II IR emission lines have a broad (∼6000 km s^{-1}) component. Contrary, the velocities of the broad components in all H I lines do not surpass 5000 km s^{-1}.

While such a velocity agrees with the average bulk ejecta velocities of most CCSNe (C. P. Gutiérrez et al. 2017), the velocities inferred from the Balmer lines of SN 2009ip (A. Pastorello et al. 2013, ∼10,000 km s^{-1}) and SN 2016jbu (C. D. Kilpatrick et al. 2018; S. J. Brennan et al. 2022b; ∼7000 km s^{-1}) are higher. Furthermore, all H I and the He I λ5016 lines have narrow emission lines (∼600–200 km s^{-1}). Such narrow lines are characteristic of classical SNe IIn/Ibn, such as SN 2010jl (C. Gall et al. 2014) and SN 2006jc, and originate from an extended CSM. However, most He I lines in the spectra of SN 2021foa lack a narrow emission component.

Figure 13 visualizes the velocity evolution of Hα and He I λ5876 of SN 2021foa in comparison to a sample of He-rich stripped-envelope SNe Ib and IIn/Ibn and SNe Ibn from Y.-Q. Liu et al. (2016) and G. Hosseinzadeh et al. (2017). Evidently, the velocities measured for SN 2021foa are inconsistent with those measured for these individual SN types.

SN 2021foa should be considered a hybrid helium-hydrogen-rich CSM interacting SN, and points to the diversity of the class of transitional SNe IIn/Ibn. This diversity ultimately arises from the myriad of mass-loss histories of massive stars. SN 2021foa's precursor emission, together with our detailed photometric and spectroscopic record for SN 2021foa allows us to further constrain the properties of the progenitor environment.

5.1. The Origin of Strongly Blueshifted Emission Lines

The most intriguing spectroscopic signature of SN 2021foa is the persistent blueshift of the peak of all H I and He I λ5016 emission lines past +66 days (Figure 14). There are three possible origins of these blueshifted profiles that can either be (i) an asymmetric CSM or SN ejecta, (ii) an effect of dust extinction, or (iii) occultation by the optically thick photosphere of photons coming from a close line-forming region. We discuss each of these scenarios below. We note that a radiatively accelerated CSM has been proposed to explain blueshifted asymmetries observed in SN 2010jl (C. Fransson et al. 2014). Nevertheless, we do not consider that scenario in this work since the blueshifted profiles in SN 2021foa are persistent at late times, while the acceleration is stronger at peak luminosity (N. Smith & J. E. Andrews 2020).

5.1.1. Asymmetric CSM

An asymmetric geometry of either the CSM or the ejecta can lead to strongly blue/redshifted emission line profiles, as has been suggested, e.g., for SNe IIn 2009ip (R. Margutti et al. 2014), 2016jbu (S. J. Brennan et al. 2022a), and 2013L (J. E. Andrews et al. 2017), SNe Ibn 2006jc (R. J. Foley et al. 2007), 2019wep (A. Gangopadhyay et al. 2022), and 2015G (I. Shivvers et al. 2017). Indeed, the presence of either an asymmetric CSM or ejecta is confirmed by spectropolarimetric observations of SNe, such as SNe IIn 1998S (D. C. Leonard et al. 2000), 2009ip (J. Mauerhan et al. 2014), 2010jl (F. Patat et al. 2011), and 2017hcc (B. Kumar et al. 2019), among others (see C. Bilinski et al. 2020, for the complete SNe IIn sample). Unfortunately, we do not have spectropolarimetric observations for SN 2021foa, and cannot conclusively confirm or rule out an asymmetric CSM/ejecta. Nevertheless, a disk-like CSM configuration is possible, with a high-density H-rich material moving toward the observer. The CSM from the receding side in this configuration has a lower density since the red emission does not rebrighten as much as the blue emission does. In this scenario, the blueshifted emission would be mostly dominated by the interaction of the SN ejecta with the dense CSM material. This

scenario has been proposed for SNe IIn PTF11iqb (N. Smith et al. 2015) to explain the highly asymmetric redshifted Hα profiles observed at $>+500$ days.

Alternatively, C. C. Thöne et al. (2017) posit that the blueshifted profiles observed in SNe IIn (SN 2009ip-like) SN 2015bh at $>+126$ days are explained as shocked emission from a single CSM shell expelled at -2000 km s^{-1} about -50 days prior to the main explosion event. Given our observations of SN 2021foa, we can compare the scenario of N. Smith et al. (2015) and the single shell suggestion for SN 2015bh (C. C. Thöne et al. 2017). Our observations indicate that the shell would need to be asymmetric in a specific direction toward the observer to produce the blueshifted profile (see Figure 14).

Furthermore, our observations, particularly the decrease in line velocities at late times, suggest that there are *multiple* H-rich CSM shells out to larger radii, rather than a single shell. Each of those shells can deviate from simple spherical symmetry. Thus, the composite of all these shells would likely lead to line profiles inconsistent with what is observed here for SN 2021foa.

While the disk-like scenario is more likely than the single shell scenario, a preexisting H-rich, high-density CSM toward the observer must also show emission at early times. However, as shown in Figure 7, the Hα line is well modeled by symmetric profiles throughout its evolution. Therefore, the high-density CSM must be placed further out of a spherical symmetric CSM.

Thus, while we cannot unambiguously rule out an asymmetric CSM as an explanation for the blueshifted line profiles without spectropolarimetry, the scenario is unlikely as it requires special fine-tuning of the CSM properties (e.g., density and location) to be consistent with our observations. Next, we consider newly formed dust and occultation by the photosphere as a potential origin of the blueshifted emission.

5.1.2. Newly Formed Dust

Newly formed dust located either close to the emission line formation region or within it causes a blueshift of the peaks of emission lines. Simultaneously, a red-blue asymmetry of the emission line profiles due to the absorption of photons from the receding side of the SN is produced (L. B. Lucy et al. 1989; C. Gall et al. 2014; A. Bevan & M. J. Barlow 2016). Thus, the blue side of the line profile remains unaffected, while the red side of the line gets extinguished (red-blue asymmetry).

Early dust formation in a cool dense shell (CDS) causing a red-blue asymmetry of emission lines has been observed in, e.g., SN 2006jc, SN 2010jl, and SN 2017hcc (e.g., N. Smith et al. 2008; N. N. Chugai 2009, 2018; C. Gall et al. 2014; A. M. Bevan et al. 2020; N. Smith & J. E. Andrews 2020). However, the newly formed dust is composed of both large and small grains (C. Gall et al. 2014; N. Smith & J. E. Andrews 2020). For the latter case, the blueshift of the emission line profiles and red-blue asymmetry exhibits a measurable wavelength dependence, with bluer emission lines exhibiting larger blueshifts than redder emission lines. As shown in Figure 14, the emission line peaks of the normalized profiles of Hα, Hβ, and Paβ for SN 2021foa are nearly identical. This rules out newly formed dust in a CDS as the origin of the blueshifted H I and He I emission lines.

Additionally, ejecta dust formation typically starts around 1 yr after explosion when the temperature of the ejecta has cooled to less than about 1600–2000 K, which are the sublimation temperatures of silicate and carbonaceous dust, respectively (C. Gall et al. 2011, and references therein). For SN 2021foa, we have a strong temperature constraint from our X-shooter modeling at late times. As shown in Table 2, the temperature of the photosphere remains at $\approx$9000 K—a factor of 4 too hot to form dust grains. Thus, ejecta dust formation can be ruled out as the origin of blueshifted emission line profiles as well as the observed NIR excess emission in SN 2021foa.

Consequently, the observed thermal dust emission (see Section 4.4) must originate from surviving preexisting dust at large distances. The amount of dust inferred from our MBB fits is consistent with dust masses derived at early epochs in other CCSNe (C. Gall et al. 2011; C. Gall & J. Hjorth 2018; W.-P. Gan et al. 2021). Further, the surviving preexisting dust must be at radii $>10^{17}$ cm, while the emission line-forming region is at lower radii ($<10^{15}$ cm). Hence, also this dust does not cause a blue-red asymmetry of the emission lines. Our observations therefore conclusively rule out newly formed dust as a source of the blueshifted line profiles.

5.1.3. Occultation by the Photosphere

Occultation can be an alternative explanation for the origin of the non-wavelength-dependent blueshifts and red-blue asymmetry of the emission line profiles of SN 2021foa. In such a scenario, the emission from the line-forming region at the receding end of the CSM/SN ejecta is occulted by the optically thick continuum photosphere (R. A. Chevalier 1976; N. Smith et al. 2012b; L. Dessart et al. 2015). This has been observed in noninteracting SNe II (J. P. Anderson et al. 2014) and suggested for some SNe IIn such as 2010jl (C. Fransson et al. 2014), 2021adxl (S. J. Brennan et al. 2024b), and 2013L (F. Taddia et al. 2020).

In the case of occultation, the line-forming region producing the intrinsically symmetric emission lines needs to be very close to the photosphere, else the effect of occultation is minimal, as discussed, e.g., for SN 2010jl, where the wavelength-dependent blueshifts are likely due to newly formed dust in the CDS (see Section 5.1.2).

For SN 2021foa, occultation is likely because we neither observe a change in the red-blue asymmetry nor blueshifts with either wavelength or time ($\sim$66–129 days). Furthermore, from our BB fits to the VLT/X-shooter data (Section 4.4), we find that the photospheric radius remains at around 2×10^{14} cm, which is similar to the location of the outer radius of the CSM using both `MOSFiT` models (Section 4.2).

However, if occultation occurs, the blueshift and red-blue asymmetry of the emission lines should decrease over time since the photosphere continues receding, blocking less photons with time. Unfortunately, we do not have any data coverage of SN 2021foa beyond $+129$ days. Thus, we cannot unambiguously determine if occultation by the photosphere is indeed a viable explanation for the observed blueshifts, but it is the most natural scenario that is consistent with all of our observations.

5.2. Precursor Emission of 2009ip-like Objects

SN 2021foa has shed off most of its hydrogen envelope, as evident from the spectra (Section 2.2). Over its lifetime, the progenitor of SN 2021foa created multiple CSM layers with

different velocities, as evident from our emission and absorption line analysis (Section 4.3, Figures 9 and 10).

The formation of multiple discrete CSM layers requires episodes of strong mass loss as eruptions or steady winds. Indeed, precursor luminous outbursts have been observed months to years before terminal explosion for SN 2006jc, SN 2015bh, and 2016jbu (R. J. Foley et al. 2007; C. C. Thöne et al. 2017; S. J. Brennan et al. 2022b).

Additionally, our high mass-loss rate estimates (2.0 $M_{\odot}$ yr^{-1}) suggest that SN 2021foa suffered from intense mass loss prior to explosion. Our analysis of the ATLAS *o*-band light-curve data from ∼5 yr prior to the SN 2021foa terminal explosion (Appendix B) shows that SN 2021foa had no eruption brighter than 20 mag over 5 yr prior to explosion. Under the $s = 2$ scheme, MOSFiT gives an outer radius of the CSM of $\approx 1.5 \times 10^{14}$ cm. Assuming a wind velocity of 400 km s^{-1}, all the CSM was expelled ∼12 yr ago, during a period of approximately half a year. Given the lack of observations of SN 2021foa prior to the year 2019, we cannot confirm such an event. However, SN 2015bh showed numerous outbursts throughout 20 yr before event B in 2015 (C. C. Thöne et al. 2017).

Several possibilities to explain the precursor emission of 2009ip-like objects have been suggested. For SN 2009ip, J. C. Mauerhan et al. (2013) argued that the explosion occurred at the onset of event A as a weak SNe II, while the brighter outburst is mainly powered by SN ejecta–CSM interaction. A similar scenario was suggested for SN 2015bh (N. Elias-Rosa et al. 2016). In contrast, A. Pastorello et al. (2013) and R. Margutti et al. (2014) have proposed that event A of SN 2009ip is an eruption similar to those observed in the years before. Then, event B is either due to the interaction of the material expelled at event A with previous eruptions (colliding shells) or the expanding SN ejecta itself (terminal explosion). Shell–shell interaction is one of the suggested scenarios to explain the precursor emission of SN 2015bh (C. C. Thöne et al. 2017).

For SN 2021foa, our MOSFiT calculations were only performed for event B photometry, i.e., assuming that the true CC-SN occurred at the end of event A, and that interaction with one CSM (RD+CSM) is sufficient to reproduce the light curve. Based on these assumptions, the low ^{56}Ni mass obtained with MOSFiT, typical for SN 2009ip-like SNe, suggests that event B is most likely powered by shock breakout of the CSM + SN ejecta–CSM interaction rather than only RD.

6. Building a Complete Picture of SN 2021foa

In this section, we summarize the key features from Section 5 and build a complete, cohesive model for SN 2021foa.

1. SN 2021foa resembles 2009ip-like SNe (A. Reguitti et al. 2022). In particular, the precursor emission (event A) of SN 2021foa starting about ∼−50 days prior to the peak of the light curve (event B) and the presence of a short plateau of a few days after the peak are very similar to SNe 2016jbu (C. D. Kilpatrick et al. 2018; S. J. Brennan et al. 2022b) and 2009ip (A. Pastorello et al. 2013; R. Margutti et al. 2014).
2. For SN 2021foa, the velocity of the minimum of the narrow absorption component of H I, He I, Fe II, Ca II, and O I lines decreases from ∼600 at day +15 to $\lesssim$300 km s^{-1} at day +60.
3. Intriguing and strongly blueshifted emission lines of H I and He I lines emerge at late times (>+66 days) in SN 2021foa.
4. SN 2021foa exhibit a distinctive phase where the He I λ5876 emission line is as strong as Hα. This line ratio plateau is observed in the transitional SNe IIn/Ibn.
5. Unambiguously, SN 2021foa has a "flip-flop" nature, transitioning from an SNe IIn before peak brightness (flip) to a He-dominated (SNe Ibn-like) SN for about +30 days, and returning to an SNe IIn past +66 days (flop).

6.1. The Luminosity of Event A and Explosion Date

As for most of the 2009ip-like events, the explosion time is uncertain and ultimately dependent on the physical mechanism employed to explain the luminosity of event A. Our spectroscopic observations strongly support a scenario where multiple CSM shells are expelled at different times prior to explosion. We sketch this scenario in Figure 15. In this scenario, the closest CSM is created by material ejected from prior outbursts or the terminal explosion. Consequently, this material is close to the progenitor system and is rapidly overrun by the forward shock from the SN, powering the emission at event A.

This scenario requires that the explosion date be at event A. For convenience, we place the assumed explosion at ≈−25 days, consistent with our results from MOSFiT fits (Table 1), and the lack of prior outbursts (see Section 5.2). We stress that the final scenario is not dependent on the precise explosion date. Even in the scenario that the outburst occurred earlier than event A, the key feature of our model for SN 2021foa is that event B itself is powered by SN ejecta–CSM interaction rather than RD.

6.2. The Dynamics of the Forward Shock from Event B to the Plateau

The broad components of H I, He I, and Ca II IR emission lines suggest an ejecta velocity of ∼6000 km s^{-1}. The maximum velocity inferred from the blue wings of the broad component, indicative of the shock velocity ($v_{\rm FS}$), does not surpass 10,000 km s^{-1} at all epochs. Therefore, we assume the velocity of the forward shock as $v_{\rm FS} = 10{,}000$ km s^{-1}. The first estimate of the photospheric radius is at $\approx 6 \times 10^{14}$ cm at day −10. At this epoch, the forward shock is located at $\approx 10^{15}$ cm. Hence, the photosphere lies within a shocked CSM region. The interaction between the SN forward shock and this close CSM might be the underlying powering mechanism of event A. Before peak, we only observe emission from the H-rich CSM, thus explaining the weak He I lines in the spectra. From −10 up to +30 days, the P Cygni profile of the Balmer lines suggests a velocity of the inner CSM layer (Figure 15) to be 600 km s^{-1}. Around day +15, the photospheric radius reaches its maximum ($\approx 10^{15}$ cm), while the forward shock is located at $\approx 3.5 \times 10^{15}$ cm. Around this epoch, we observe the "flip"; the He-rich ejecta is becoming visible, and He I lines get stronger.

6.3. Evolution Post-plateau to Late Time

After the plateau phase (+25 days), the photospheric radius starts to recede to a radius of about 6×10^{14} cm. In the

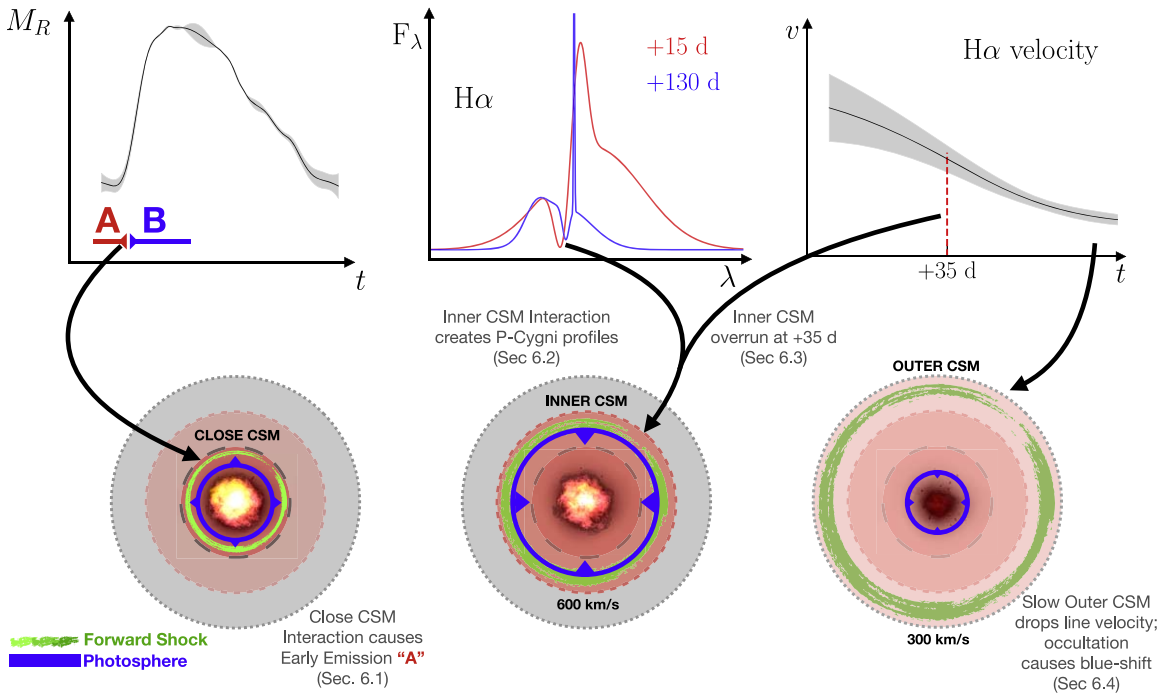

Figure 15. Proposed scenario for SN 2021foa, sketching the temporal evolution of the forward shock and the photospheric radius. In this scenario, SN 2021foa is embedded in a H-rich CSM composed of multiple shells. The precursor emission (event A) originated from the interaction of the SN forward shock with an unobserved, close CSM. From day −10 to +35, a second inner CSM with a characteristic velocity of ≈600 km s^{-1} is observed through the P Cygni profile of the Balmer lines. The He-rich ejecta, hidden at early epochs, is visible at day +15 after the photospheric radius reaches its maximum. The strong He I lines at this epoch sets up the "flip" in Figure 12. A rapid decline of the Hα velocity at day +35 marks the phase where the forward shock overran most of the inner CSM. After day +50, the velocity of the Hα line remains constant at ≈350 km s^{-1}. We attribute this velocity to an outer CSM shell. The rebrightening of Balmer lines at late times (+66–+130 days) due to hydrogen recombination of a shocked SN ejecta–CSM (either the close, inner, or outer CSM), gives rise to the "flop" in Figure 12. The apparent blueshift of several lines at late times is either due to an asymmetric CSM or an effect of occultation by the optically thick photosphere close to the line-forming region of these lines, located at ∼2 × 10^{14} cm.

meanwhile, the forward shock continues to propagate outward, reaching a radius of about 5 × 10^{15} cm, assuming a constant forward shock velocity. At day +35, we first observe the decline of the velocity of the absorption minimum of the Balmer lines (H I in Figure 10). This decline implies that the forward shock has overrun the inner CSM entirely. Nevertheless, though weaker, the continuous interaction between the SN ejecta and the CSM still powers the emission of H I and He I lines (Figure 11). This is evident in the plateau phase of the Hα/He I λ5876 ratio (Figure 12).

Past +50 days, the line fluxes of H I lines, from Hδ to Paβ, increase (or stay constant), while He I lines keep decreasing (Figure 11). At this epoch, we observe the "flop" in Figure 12.

6.4. Late-time Evolution

At +130 days, the velocities of the absorption minima of H I, He I, Ca II, O I, and Fe II are below ∼350 km s^{-1}. This is consistent with a slow-moving outer CSM layer at a distance of >1.3 × 10^{16} cm, and thus, has not been overrun yet by the forward shock ($v_{FS} = 10^4$ km s^{-1}). The likely origin of the low-velocity outer CSM is from slow winds at early stages in the evolution of the progenitor star, while the inner CSM shells are from eruptions or faster winds closer to the explosion. In the multiple shells scenario, the slowly receding photosphere (∼2 × 10^{14} cm from +60 to +130 days) lies within the inner CSM, close to the line-forming region of the intermediate/broad components (≈4000 km s^{-1}). In this scenario, the blueshifted emission lines emerging after the plateau phase are the result of occultation (Section 5.1.3) of the emission line region by a dense and optically thick CSM shell. Finally, at late times, the H-rich inner CSM recombines, explaining the rebrightening of the Balmer lines (Figure 11). Alternatively, as suggested for PTFiqb (N. Smith et al. 2015), the interaction between the SN ejecta and a dense, outer CSM approaching to the observer at −2000 km s^{-1}, could also be a viable option to explain the late rebrightening and asymmetry observed in the H I lines.

6.5. Final Remarks

The early discovery and follow-up of SN 2021foa exhibit the imprints of CSM interaction on the SN's light curve and the evolution of its spectral features. From our light-curve analysis (Section 4.2), we obtain a CSM mass ⩽1 $M_\odot$, ejecta mass ≈8 $M_\odot$, and mass-loss rate of 2 $M_\odot$ yr^{-1} for a wind-like ($s = 2$) scenario. This mass-loss rate is higher than values typically found for W-R or LBV stars, favored progenitors of SNe Ibn/IIn, respectively. From our detailed analysis of the evolution of the line profiles (Section 4.3), we conclude that SN 2021foa had a rich mass-loss history, forming multiple CSM shells before the terminal explosion. This CSM configuration, while rare, does share key similarities with other scenarios proposed for interacting SNe, such as SN 2015bh (N. Elias-Rosa et al. 2016). We stress that the assumption of a one-shell CSM in `MOSFiT` is insufficient to explain the precursor emission of SN 2021foa and is incompatible with a CSM composed of multiple shells. Nevertheless, the overall behavior of the light curve during event B might be approximated well by this assumption. Therefore, the estimated `MOSFiT` physical parameters might

still be valid if the interaction with the close/inner CSM in our scenario is the main contributor to the luminosity of event B.

SN 2021foa adds to the number of SNe with truly complex CSM structures, which challenges our understanding of extreme mass-loss mechanisms in massive stars, opening up the possibilities of different progenitor scenarios for strongly interacting CCSNe.

Acknowledgments

We thank S. Raimundo, O. Rodriguez, and the anonymous referee for constructive comments that helped to improve the manuscript.

This work is supported by a VILLUM FONDEN Young Investigator Grant (project number 25501) and by research grants (VIL16599, VIL54489) from VILLUM FONDEN. C.R. A. is supported by the European 1172 Research Council (ERC) under the European Union's 1173 Horizon 2020 research and innovation program (grant 1174 agreement No. 948381). V.A. V. acknowledges support from the National Science Foundation (NSF) through grant AST–2108676. This work is supported by the NSF under Cooperative Agreement PHY-2019786 (The NSF AI Institute for Artificial Intelligence and Fundamental Interactions, http://iaifi.org/). Parts of this research were supported by the Australian Research Council Discovery Early Career Researcher Award (DECRA) through project No. DE230101069. The UCSC team is supported in part by NASA grant 80NSSC20K0953, NSF grant AST-1815935, the Gordon and Betty Moore Foundation, the Heising-Simons Foundation, and by a fellowship from the David and Lucile Packard Foundation to R.J.F. R.Y. received support from a Doctoral Fellowship from the University of California Institute for Mexico and the United States (UCMEXUS) and a NASA FINESST award (21-ASTRO21-0068) postdoctoral fellowship. G.N. gratefully acknowledges NSF support from AST-2206195 for this work. G.N. is also supported by NSF CAREER grant AST-2239364, supported in part by funding from Charles Simonyi, and NSF OAC-2311355, DOE support through the Department of Physics at the University of Illinois, Urbana-Champaign (13771275), and support from the HST Guest Observer Program through HST-GO-16764 and HST-GO-17128 (PI: R. Foley). This work was performed in part at the Aspen Center for Physics, which is supported by NSF grant PHY-2210452.

This investigation is based on observations made with ESO Telescopes at the La Silla Paranal Observatory under program ID 107.22RH (PI: C. Gall) and 109.23K3 (PI: D. Farias). Research at Lick Observatory is partially supported by a generous gift from Google. Based in part on observations obtained at the SOAR telescope, which is a joint project of the Ministério da Ciência, Tecnologia e Inovações (MCTI/LNA) do Brasil, the US National Science Foundation's NOIRLab, the University of North Carolina at Chapel Hill (UNC), and Michigan State University (MSU). The data presented here were obtained in part with ALFOSC, which is provided by the Instituto de Astrofisica de Andalucia (IAA) under a joint agreement with the University of Copenhagen and NOT. We acknowledge the use of public data from the Swift data archive. This work makes use of data taken with the Las Cumbres Observatory global telescope network. The LCO group is funded by NSF grants AST-1911151 and AST-1911225. This work has made use of data from the ATLAS project. ATLAS is primarily funded to search for near-Earth asteroids through NASA grants NN12AR55G, 80NSSC18K0284, and 80NSSC18K1575; byproducts of the NEO search include images and catalogs from the survey area. The ATLAS science products have been made possible through the contributions of the University of Hawaii Institute for Astronomy, the Queen's University Belfast, and the Space Telescope Science Institute. This work is based in part on data obtained at the Infrared Telescope Facility, which is operated by the University of Hawaii under contract 80HQTR24DA010 with NASA.

YSE-PZ was developed by the UC Santa Cruz Transients Team. The UCSC team is supported in part by NASA grants NNG17PX03C, 80NSSC19K1386, and 80NSSC20K0953; NSF grants AST-1518052, AST-1815935, and AST-1911206; the Gordon & Betty Moore Foundation; the Heising-Simons Foundation; a fellowship from the David and Lucile Packard Foundation to R.J.F.; Gordon and Betty Moore Foundation postdoctoral fellowships and a NASA Einstein Fellowship, as administered through the NASA Hubble Fellowship program and grant HST-HF2-51462.001, to D.O. J.; and an NSF Graduate Research Fellowship, administered through grant DGE-1339067, to D.A.C.

Facilities: Swift (UVOT), LCOGT (Sinistro), Shane (Kast, Nickel), VLT:Kueyen (X-shooter), NOT (ALFOSC), ATT (WiFeS), SOAR (Goodman), IRTF (SpeX), ATLAS, Thacher. Computational Facility: High Performance Cluster (HPC) of the University of Copenhagen.

Software: Astropy (Astropy Collaboration et al. 2013, 2018), `EsoReflex` (W. Freudling et al. 2013), `extrabol` (I. Thornton & V. A. Villar 2022), `SuperBol` (M. Nicholl et al. 2017), `matplotlib` (J. D. Hunter 2007), `MOSFiT` (J. Guillochon et al. 2018), `NumPy` (C. R. Harris et al. 2020), `specutils` (N. Earl et al. 2023), YSE-PZ (D. A. Coulter et al. 2022).

Appendix A
Host Emission at Hα

The narrow emission component of Balmer lines in the VLT/X-shooter spectra is dominated by the host galaxy emission rather than photoionized unshocked CSM. Figure A1 demonstrates the challenge of performing an accurate reduction at the spectral range covering Hα profile due to the contamination of the host emission. Despite special efforts to correctly address this issue, the line flux of Hα (Figure 11) at +95 days might be overestimated.

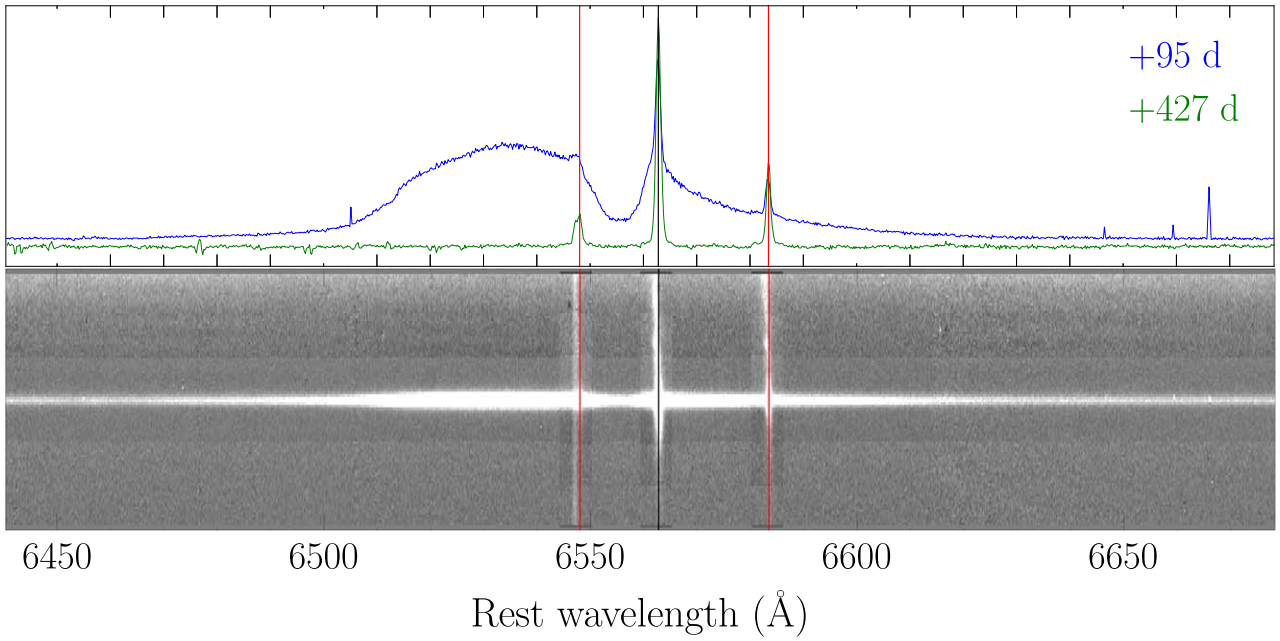

Figure A1. VLT/X-shooter spectral region surrounding Hα of SN 2021foa. Upper panel: spectra at +95 and +427 days past peak. The black and red lines are located at the rest wavelength of Hα and [N II] $\lambda\lambda$6548, 6583, respectively. Bottom panel: the 2D spectrum at day +95 within the same spectral region.

Table A1
Photometry of SN 2021foa

MJD	Filter	Magnitude	Error	System	Instrument	Telescope
58147.50	*o*	19.046	0.264	AB	ACAM1	ATLAS
58295.50	*o*	19.403	0.357	AB	ACAM1	ATLAS
59019.50	*o*	18.336	0.303	AB	ACAM1	ATLAS
59267.50	*o*	19.224	0.291	AB	ACAM1	ATLAS
59271.50	*o*	19.102	0.297	AB	ACAM1	ATLAS
59272.50	*o*	19.351	0.288	AB	ACAM1	ATLAS
59277.50	*o*	19.268	0.318	AB	ACAM1	ATLAS
59279.50	*o*	19.111	0.190	AB	ACAM1	ATLAS
59288.50	*o*	16.002	0.018	AB	ACAM1	ATLAS
59289.26	*UVW*1	15.139	0.050	Vega	UVOT	Swift
59289.27	*U*	14.820	0.043	Vega	UVOT	Swift
59289.27	*B*	15.916	0.060	Vega	UVOT	Swift
59289.29	*UVW*2	15.957	0.061	Vega	UVOT	Swift
59289.29	*V*	15.678	0.086	Vega	UVOT	Swift
59289.33	*U*	15.573	0.078	Vega	UVOT	Swift
59290.79	*UVW*2	15.790	0.049	Vega	UVOT	Swift
59290.79	*V*	15.419	0.078	Vega	UVOT	Swift
59290.79	*U*	15.356	0.049	Vega	UVOT	Swift
59290.79	*U*	14.605	0.043	Vega	UVOT	Swift
59290.80	*UVW*1	14.958	0.048	Vega	UVOT	Swift
59290.80	*B*	15.759	0.067	Vega	UVOT	Swift
59290.87	*gp*	15.558	0.016	AB	Sinistro	LCO
59290.87	*rp*	15.649	0.017	AB	Sinistro	LCO
59290.87	*ip*	15.803	0.021	AB	Sinistro	LCO
59291.52	*B*	15.591	0.019	AB	Sinistro	LCO
59291.52	*V*	15.343	0.015	AB	Sinistro	LCO
59291.52	*R*	15.394	0.014	AB	Sinistro	LCO
59291.64	*UVW*2	15.715	0.054	Vega	UVOT	Swift
59291.65	*U*	14.439	0.045	Vega	UVOT	Swift
59291.65	*U*	15.316	0.054	Vega	UVOT	Swift
59291.65	*B*	15.667	0.079	Vega	UVOT	Swift
59291.65	*V*	15.220	0.085	Vega	UVOT	Swift
59291.65	*UVW*1	14.837	0.051	Vega	UVOT	Swift

(This table is available in its entirety in machine-readable form in the online article.)

Table A2
Spectroscopy of SN 2021foa

Date	Phase (days)	Coverage (Å)	Dispersion (Å)	Instrument	Telescope
2021-03-18	−11	3768–6939	0.76–1.24	WiFeS	ANU
2021-03-18	−11	5680–8580	1.4	ALFOSC	NOT
2021-03-21	−8	3877–7037	1.98	Goodman	SOAR
2021-03-21	−8	6845–25485	1.19–3.55	SpeX	IRTF
2021-03-22	−7	3345–10504	2.51	Kast	Shane
2021-03-22	−7	3768–8923	3.35	ALFOSC	NOT
2021-03-23	−6	5680–8580	1.4	ALFOSC	NOT
2021-04-06	+8	3345–10504	2.51	Kast	Shane
2021-04-10	+12	6845–25485	1.19–3.55	SpeX	IRTF
2021-04-13	+15	3345–10504	2.51	Kast	Shane
2021-04-19	+21	3345–10504	2.51	Kast	Shane
2021-05-03	+35	3345–10504	2.51	Kast	Shane
2021-05-09	+41	7091–25485	1.19–3.55	SpeX	IRTF
2021-05-10	+42	3345–10504	2.51	Kast	Shane
2021-05-19	+51	3768–6939	0.76–1.24	WiFeS	ANU
2021-05-10	+51	3345–10504	2.51	Kast	Shane
2021-06-03	+66	2964–24583	0.19–0.59	X-shooter	VLT
2021-07-02	+95	2964–24583	0.19–0.59	X-shooter	VLT
2021-08-04	+129	2964–24583	0.19–0.59	X-shooter	VLT
2022-05-30	+427	2964–24583	0.19–0.59	X-shooter	VLT

Table A3
Full Width at Half-maximum of H I and He I Lines of SN 2021foa

Epoch	Narrow				Absorption				Broad					
(days)	Hδ	Hγ	Hβ	Hα	Hδ	Hγ	Hβ	Hα	Hδ	Hγ	Hβ	Hα	Paβ	He I λ5876
−11/10	⋯	⋯	1.4(1.2)	3.7(0.1)	⋯	⋯	4.3(1.0)	⋯	⋯	⋯	23.5(3.1)	14.9(1.0)	⋯	⋯
−3	⋯	⋯	8.6(1.0)	5.5(1.0)	⋯	⋯	8.7(1.0)	6.4(0.2)	⋯	⋯	39.5(8.6)	40.3(3.0)	⋯	⋯
+7/8	⋯	⋯	2.0(1.7)	4.6(0.4)	⋯	⋯	4.3(1.0)	6.7(0.3)	⋯	⋯	25.6(2.2)	40.3(1.3)	⋯	64.8(–)
+15	⋯	⋯	2.7(1.2)	6.5(0.6)	⋯	⋯	6.6(0.4)	7.1(0.4)	⋯	⋯	32.2(2.0)	46.1(1.6)	⋯	61.8(–)
+21	⋯	⋯	2.4(4.7)	5.4(0.8)	⋯	⋯	11.1(1.3)	6.7(0.4)	⋯	⋯	32.0(2.4)	48.7(1.3)	⋯	56.7(–)
+28	⋯	⋯	8.0(1.0)	5.9(1.0)	⋯	⋯	8.0(1.0)	5.9(0.8)	⋯	⋯	27.7(3.6)	50.3(0.6)	⋯	55.0(–)
+35/36	⋯	⋯	2.2(5.7)	2.0(0.1)	⋯	⋯	6.2(0.2)	8.5(0.4)	⋯	⋯	23.5(1.9)	46.8(0.4)	⋯	51.5(–)
+42/43	⋯	⋯	3.7(1.0)	1.1(0.2)	⋯	⋯	1.6(2.1)	7.6(0.4)	⋯	⋯	22.4(1.4)	48.0(0.6)	⋯	47.0(–)
+51	⋯	⋯	⋯	1.4(0.1)	⋯	⋯	⋯	5.4(0.7)	⋯	⋯	⋯	41.6(1.0)	⋯	43.5(–)
+66	0.6(0.1)	0.4(0.1)	0.2(0.1)	0.6(0.0)	4.0(0.9)	3.0(0.2)	3.0(0.2)	3.4(0.1)	21.7(1.1)	27.6(1.1)	24.2(0.4)	36.2(0.4)	32.3(0.7)	47.6(–)
+95	0.6(0.1)	0.4(0.2)	0.4(0.0)	0.7(0.0)	3.7(0.5)	3.0(0.1)	3.0(0.2)	3.3(0.1)	19.7(0.9)	21.4(0.6)	21.7(0.3)	29.3(0.2)	28.7(0.6)	46.1(–)
+129	0.2(0.1)	0.4(0.0)	0.4(0.0)	0.4(0.0)	5.1(0.4)	2.9(0.2)	3.4(0.1)	3.3(0.2)	9.3(0.8)	21.2(1.0)	17.0(0.8)	26.0(0.4)	25.1(1.0)	⋯

Note. Values of the FWHM are in units of 100 km s^{-1}. All values are corrected by the resolution of the instrument (≈dispersion in Table A2). Given the complexity of He I λ5876 line profile, only upper limits are reported.

Table A4
Fitted Absorption Minimum of Several Spectral Lines of SN 2021foa

Epoch (days)	H I				He I		Fe II			Ca II			O I
	Hδ	Hγ	Hβ	Hα	λ4923	λ5016	λ5169	λ5276	λ5317	λ8498	λ8542	λ8662	λ8446
−10	3.5(1.2)	3.3(1.1)	4.1(1.0)	⋯	4.2(1.0)	3.1(1.0)	⋯	⋯	⋯	⋯	⋯	⋯	⋯
−3	⋯	⋯	6.6(1.9)	5.9(1.4)	4.2(1.8)	3.4(1.8)	⋯	⋯	⋯	⋯	⋯	⋯	⋯
+7/8	3.6(1.2)	3.7(1.1)	5.3(1.0)	5.6(1.1)	4.0(1.0)	⋯	⋯	⋯	⋯	⋯	3.3(0.9)	3.9(0.9)	2.8(0.9)
+15	⋯	⋯	5.9(1.6)	5.1(1.1)	3.8(1.5)	3.3(1.5)	⋯	⋯	⋯	⋯	3.3(0.9)	2.9(0.9)	3.2(0.9)
+21	⋯	⋯	5.1(1.6)	6.2(1.1)	2.3(1.5)	⋯	⋯	⋯	⋯	⋯	⋯	⋯	⋯
+28	⋯	⋯	5.8(1.9)	6.5(1.4)	4.8(1.8)	⋯	⋯	⋯	⋯	⋯	⋯	⋯	⋯
+35/36	⋯	⋯	5.9(1.6)	4.8(0.4)	2.2(1.5)	4.0(1.5)	⋯	⋯	⋯	⋯	3.1(0.9)	2.8(0.9)	2.8(0.9)
+42/43	⋯	⋯	4.2(1.6)	4.0(0.5)	1.2(1.5)	1.9(1.5)	⋯	⋯	⋯	2.3(0.9)	2.2(0.9)	2.6(0.9)	3.4(0.9)
+66	2.2(0.1)	2.9(0.1)	2.9(0.1)	3.8(0.1)	0.9(0.1)	0.8(0.1)	1.8(0.1)	1.6(0.1)	1.6(0.1)	1.7(0.1)	2.1(0.1)	1.9(0.1)	1.3(0.1)
+95	2.7(0.1)	2.9(0.1)	2.7(0.1)	3.5(0.1)	1.1(0.1)	0.7(0.1)	2.0(0.1)	1.8(0.1)	1.8(0.1)	1.7(0.1)	2.1(0.1)	1.9(0.1)	1.4(0.1)
+129	3.2(0.1)	2.7(0.1)	2.7(0.1)	3.5(0.1)	1.1(0.1)	1.5(0.1)	2.1(0.1)	0.7(0.1)	1.8(0.1)	1.8(0.1)	2.1(0.1)	1.8(0.1)	1.5(0.1)

Note. Values of the absorption minimum are reported in units of -100 km s^{-1}. Uncertainties are estimated as $c \cdot \Delta\lambda_D/\lambda_0$, with c the speed of light, $\Delta\lambda_D$ the dispersion of the instrument in Table A2, and λ_0 the center of the Gaussian profile.

Table A5
Line Fluxes of H I and He I Lines of SN 2021foa

Epoch (days)	Hδ	Hγ	Hβ	Hα	Paβ	He I λ5876	He I λ7065
−11/10	29.3(2.4)	40.7(2.6)	46.4(4.7)	86.9(7.3)	⋯	25.6(–)	⋯
−8/7	⋯	⋯	52.2(3.6)	105.6(15.6)	⋯	35.9(–)	14.3(1.3)
−3	⋯	⋯	77.7(4.4)	105.7(11.6)	⋯	40.3(–)	⋯
+7/8	24.6(2.2)	37.2(3.0)	54.2(3.3)	131.3(16.3)	⋯	129.2(–)	48.1(1.7)
+15	⋯	⋯	35.9(11.4)	120.0(15.7)	⋯	138.5(–)	59.7(1.8)
+21	⋯	⋯	43.4(18.1)	139.0(15.8)	⋯	137.1(–)	60.3(2.0)
+28	⋯	⋯	19.1(8.0)	121.2(14.7)	⋯	96.4(–)	69.8(1.8)
+35/36	⋯	⋯	11.2(4.8)	59.9(16.7)	⋯	61.3(–)	32.8(0.7)
+42/43	⋯	⋯	10.9(5.5)	56.0(16.7)	⋯	39.9(–)	24.5(0.5)
+51	⋯	⋯	⋯	31.7(20.9)	⋯	32.0(–)	19.8(1.1)
+66	0.8(0.0)	1.7(0.1)	6.4(0.1)	38.0(0.1)	3.8(0.0)	14.3(–)	9.3(0.0)
+95	0.5(0.0)	1.2(0.0)	5.9(0.0)	38.4(0.1)	3.5(0.0)	5.9(–)	3.2(0.0)
+129	0.3(0.0)	1.0(0.0)	5.5(0.1)	31.3(0.1)	3.7(0.0)	1.7(–)	2.0(0.0)

Note. Values are reported in units of 10^{-17} erg s^{-1} cm^{-2}. Line fluxes of He I λ5876 correspond to the integration of the data over $\approx \pm 5000$ km s^{-1} with respect to 5876 Å.

Appendix B
Pre-SN Emission

To investigate the pre-explosion activity of SN 2021foa, we followed the analysis described in Q. Wang et al. (2024) using `ATClean` (S. Rest et al. 2023, 2024). We obtain the ATLAS forced photometry of the o and c bands covering ∼5 yr up to event A at the position of SN 2021foa. Additionally, we performed forced photometry of eight control light curves within a distance of 17″ to the SN. On average, the flux of these control light curves is expected to be zero. To emphasize the emission of a potential eruption, we defined a figure of merit (FOM) as the SNR convolved with a rolling Gaussian with a fixed kernel size determined by the typical timescale of an eruption, $5 < \tau_G < 100$ days (E. O. Ofek et al. 2013b; N. L. Strotjohann et al. 2021). The same rolling Gaussian was also applied to the control light curves to determine the FOM of the control light curves. By setting up a detection threshold $\mathrm{FOM_{limit}}$, we expect that most of the FOM of the control light curves lies below this limit. If this is not the case, then there are unaccounted sources of contamination within the field of SN 2021foa. Any real detection in the pre-SN light curve must have an FOM larger than the $\mathrm{FOM_{limit}}$. In order to establish a magnitude limit to detect eruptions of a given peak magnitude, we added three simulated Gaussian bumps (p_1, p_2, and p_3) with increasing amplitudes to one control light curve. A nondetection of any of these peaks translates into an upper limit of a real pre-SN eruption throughout the ATLAS coverage.

For the particular case of SN 2021foa, we first convolved both the SNR of the control and SN light curves with a rolling Gaussian with a kernel size of $\tau_G = 30$ days, close to the duration of the precursor emission observed in SN 2021foa. Furthermore, we added three simulated Gaussian bumps, with peak magnitudes of $p_1 = 21.4$, $p_2 = 20.21$, and $p_3 = 19.45$ mag, and a fixed standard deviation of 25 days to the control light curve number 4. Finally, we set up the detection limit as $\mathrm{FOM_{limit}} = 15$. With this same value, Q. Wang et al. (2024) recovered 80% of the eruptions larger than 20 mag for SNe Ibn 2020nxt. For SN 2021foa, we recover 70% of the eruptions larger than the o-band peak magnitude ≈20 mag.

The upper panel of Figure B1 displays the forced photometry ATLAS light curves for SN 2021foa (red) and the control light curves (cyan and blue). We find no signature of any precursor emission associated with SN 2021foa. The bottom panel shows

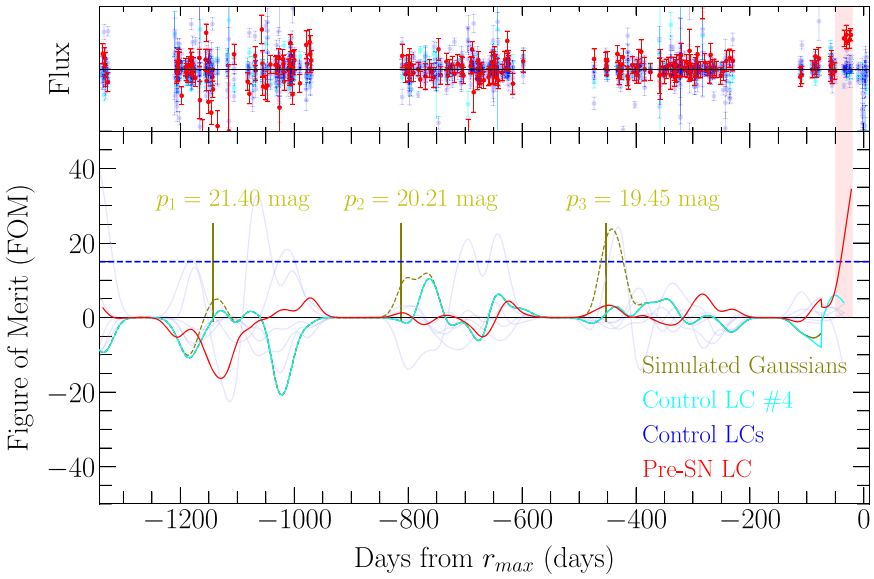

Figure B1. Upper panel: the light curve of SN 2021foa (red) and the eight control light curves (blue) before event A (red). Bottom panel: FOM of the pre-SN light curve (red), eight control light curves (blue), control light curve number 4 (cyan), and the simulated Gaussians + control light curve number 4 (green) over ATLAS coverage (∼3 yr) up to event A of SN 2021foa. All these FOM curves were obtained after the convolution of the SNR of each light curve with a rolling Gaussian with a kernel size of $\tau_G = 30$ days. The simulated Gaussians have peak magnitudes of 21.4 mag, 20.21 mag, and 19.35 mag, respectively, and a fixed standard deviation of 15 days. The detection limit for our analysis was set up as $\mathrm{FOM_{limit}} = 15$ (dashed line). The red-shaded area encompasses the precursor emission of SN 2021foa.

the results of our detection analysis. On average, the control light curves are below $\mathrm{FOM_{limit}}$. For the simulated Gaussians, only p_3 was successfully detected, while p_2 lies slightly below the threshold. Therefore, we can safely conclude that, similar to Q. Wang et al. (2024), no eruption is observed for SN 2021foa with a magnitude greater than or equal to ∼20 mag. This translates into a detection limit of absolute magnitude of $M_o \approx -13.4$ mag. However, we cannot discard any pre-SN activity below this magnitude limit.

Appendix C
Line Profiles

C.1. Hα

Panel (D) in Figure C1 shows the evolution of Hα between about 1 week prior to the *r*-band peak and to +427 days. The line is characterized by a narrow (FWHM ∼ 600 km s^{-1}) and an intermediate component with an FWHM that increases from ∼1500 to 4500 km s^{-1}. After maximum light, no major changes are observed aside from a decreasing flux at the red wing of the asymmetric profile. After +60 days, the red-blue asymmetry has flipped, i.e., the blue wing has increased in strength over the red wing. The narrow emission component has faded after about +51 days, revealing the Hα host galaxy emission (FWHM $\lesssim$ 100 km s^{-1}) instead. The apparent rebrightening of the blue peak of Hα at +95 days is an artifact stemming from the extraction of the 2D spectrum at the location of Hα (see Figure A1).

C.2. Hβ

The evolution of Hβ line is shown in Panel (C) in Figure C1. The Hβ line profile is similar to Hα prior to peak magnitude. At later epochs, Hβ is blended with the strong He I λ4922 emission. Both Hβ and He I λ4922 exhibit narrow absorption lines with absorption velocities from −10 days onward (∼−600 and ∼−400 km s^{-1}, respectively). However, the narrow absorption line of He I could be partially associated with Fe II λ4924 line of multiplet 42. Similar to the Hα line, the line flux of the Hβ + He I λ4922 complex reaches a maximum around +15 days and decreases between +28 and +66 days. After this epoch, Hβ shows a strong blueshifted emission component, while the velocity of the minimum of the absorption component reaches ∼300 km s^{-1}. The emission of He I λ4922 is weak in comparison to Hβ, allowing us to disentangle both lines at these late epochs. Similar to Hα and Hβ, He I λ4922 also exhibits a blueshifted emission component.

C.3. He I λ5016

In panel (G) (Figure C1), we show the evolution of the He I λ5016 line. From −10 days onward, this line shows a P Cygni profile, with the absorption minimum at a velocity of ∼−400 km s^{-1}. Similarly to He I λ4922, the narrow absorption component can be associated with Fe II λ5018 of multiplet 42. The extension of the wings of the broad emission component may indicate a maximum velocity of 4000 km s^{-1} (bulk velocity of ∼3000 km s^{-1}). After maximum light, the shape of the profile is broad and boxy-like. Assuming one component, the FWHM of this complex is about 3600 km s^{-1}. This is consistent with what is seen for Hα. From +95 days onward, the flux at the red portion of the He I λ5016 emission line profile rapidly decreases. The region might be affected at early times by the emission of He I λ5048.

C.4. He I λ5876

Panel (H) in Figure C1 displays the evolution of He I λ5876, which is the strongest of all He I lines in the entire VLT/X-shooter spectral wavelength range. There is no indication of a narrow P Cygni profile as in other He I λλ4922, 5016 lines. However, there is conspicuous, redshifted absorption at all epochs up to +129 days, which likely is the Na ID doublet from interstellar material along the line of sight. The emission line profile appears symmetric at early epochs (2 weeks past

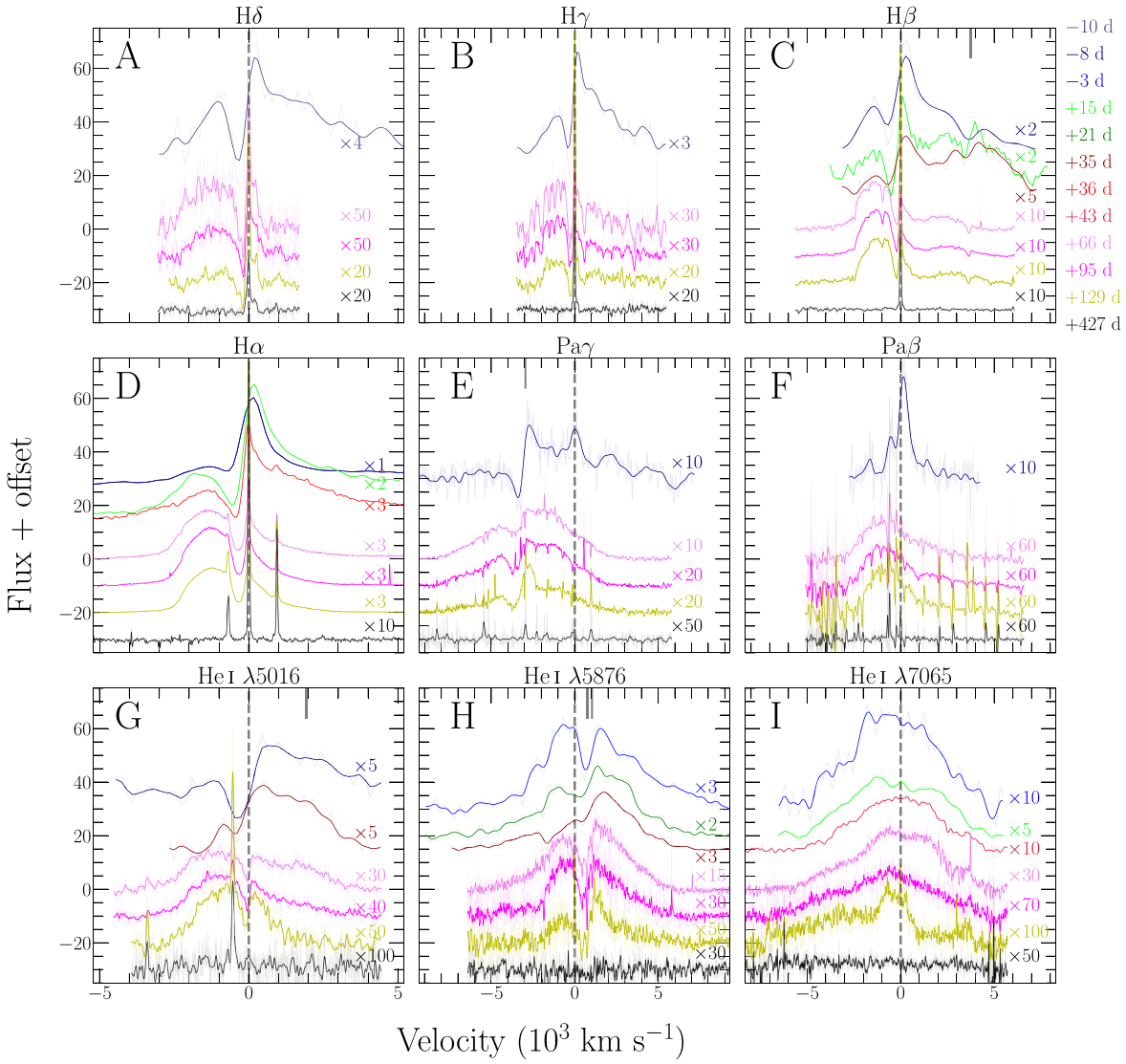

Figure C1. Evolution of the the most prominent continuum-subtracted H I and He I lines of SN 2021foa. Dashed, vertical lines correspond to zero velocity. Solid, vertical lines in panels (C), (E), (G), and (H) correspond to the velocities at the wavelengths of He I λλ4922, 5048, 10830 and Na ID, respectively.

maximum) in comparison to H I lines. Thereafter, the line develops a redshifted peak. From about +66 days onward, it appears symmetric again, unlike other He I and H I lines.

C.5. He I λ7065

In panel (I) in Figure C1, we show the evolution of He I λ7065. In analogy to He I λ5876, the emission line profile of He I λ7065 is of boxy-like shape with no evident narrow P Cygni profile. Additionally, at all epochs, the line profile exhibits a blue shoulder at around −3000 km s^{-1}. The origin of both emission features is unclear but may be due to another element.

C.6. NIR Lines

The NIR spectra exhibit emission lines of He I λ10830 + Paγ, Paβ and He I λ20581. H I λ18751 (Paα) is detected, but it coincides with a telluric region. Panel (E) in Figure C1 shows the He I λ10830 + Paγ line complex, which is dominated by He I λ10830. We find that the absorption line at about −4000 km s^{-1} (with reference to Paγ) must be attributed to He I λ10830. This is because it is unlikely that a narrow Paγ absorption at a velocity of about −4000 km s^{-1} with an FWHM of only about 800 km s^{-1} exists. Furthermore, the velocity of the absorption minimum, if associated with He I λ10830, remains nearly constant at about −600 km s^{-1} at all epochs up to +129 days.

Panel (F) in Figure C1 displays the evolution of Paβ. At −8 days, the emission line has a FWHM of only about 2000 km s^{-1} and thus, is narrower than other H I lines at that epoch. On top of that is a narrow P Cygni profile with an FWHM of about ∼1000 km s^{-1} and an absorption component with a minimum at ∼−500 km s^{-1}. From +66 to +129 days, the Paβ line profile is nearly identical to the optical H I lines. However, Paβ does not show a narrow absorption component, likely because it coincides with telluric lines at that position.

C.7. Other Line Profiles

Another complex spectral structure is prominent in the wavelength range of Ca II H&K (λλ3934, 3968). The left panel of Figure C2 shows the evolution of this structure at +66, +95, and +129 days. The absorption complex at the position of Ca II H&K exhibit multiple components, some appear blueshifted

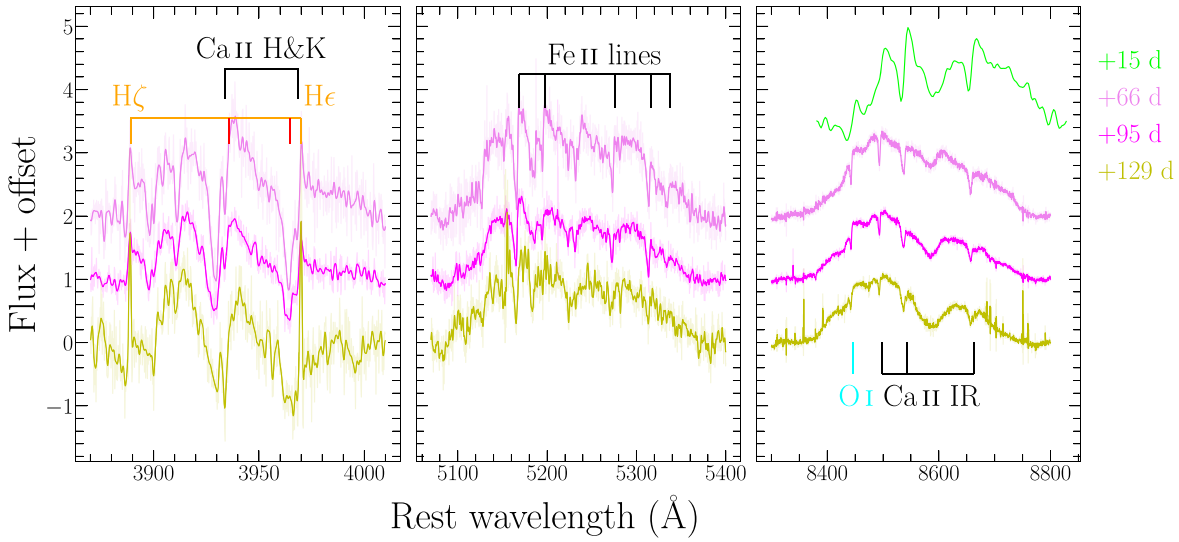

Figure C2. Left panel: evolution of the spectral region surrounding Ca II H&K. The P Cygni profile of the Balmer lines Hζ and Hϵ are prominent. Middle panel: evolution of the spectral region surrounding the pseudo-continuum produced by the blended Fe II lines. Right panel: evolution of the Ca II NIR + O I λ8446. All the regions in each panel are continuum subtracted.

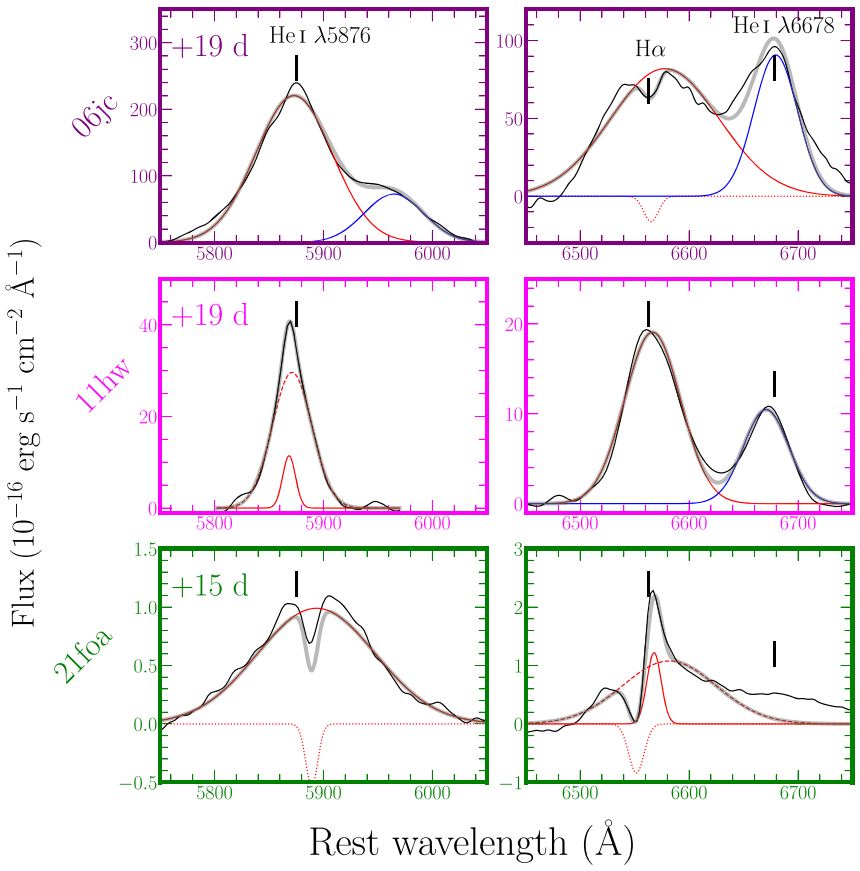

Figure C3. Decomposition of continuum-subtracted line profiles of He I λ5876 (left column) and Hα (right column) of SNe Ibn 2006jc (upper row), transitional SNe IIn/Ibn 2011hw (middle row) and 2021foa (lower row) at 2 weeks after *r*-band maximum. Solid and dashed lines represent the fits to the emission components of the line profiles, while dotted lines correspond to the fit to any absorption trough.

with respect to the SN redshift. Strong absorption features, potentially associated with these Ca II lines are at about −350 km s^{-1}. Since there is no indication of any emission or absorption lines at these wavelengths in the +427 days spectrum, it is likely that the absorption complex originates from different CSM layers around the SN. However, the mismatch between the low velocities from the absorption trough of the Ca II IR and the Ca II H&K counterparts is intriguing. This apparent discrepancy could be solved considering that Ca II H&K could be misidentified due to the strong blending with He I λλ3936, 3965 (vertical red lines in the left panel).

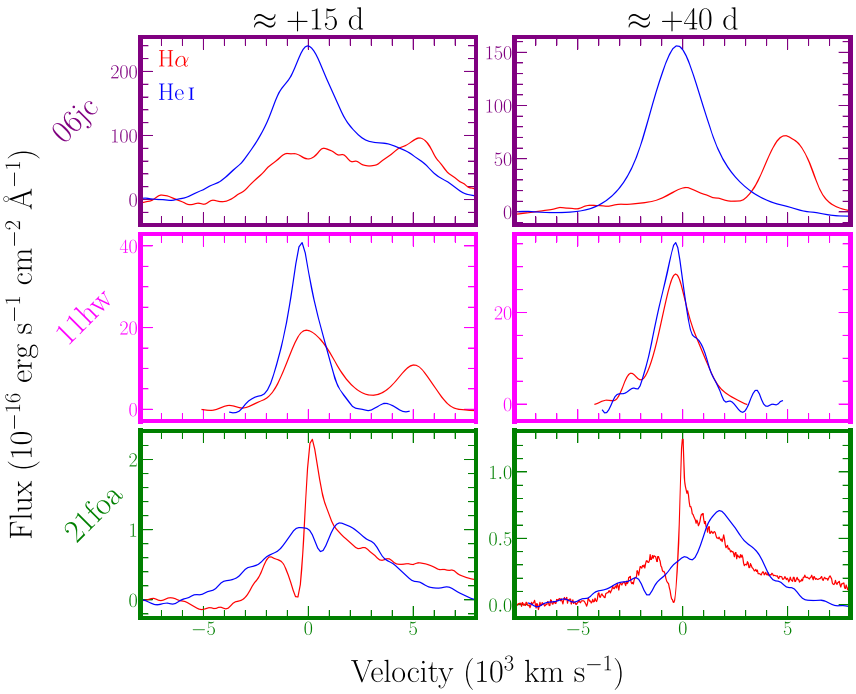

Figure C4. Comparison of continuum-subtracted line profiles of Hα (red) and He I λ5876 (blue) of SNe Ibn 2006jc (upper row), transitional SNe IIn/Ibn 2011hw (middle row), and 2021foa (lower row) at ≈15 (left column) and ≈40 (right column) days past *r*-band maximum.

Several Fe II (multiplets 42, 48, and 49) lines are shown in the middle panel in Figure C2 at +66 to +427 days. Strong blending of Fe II forest lines can create a pseudo-continuum as observed blueward of 5700 Å. This is not unusual for SNe Ibn and other interacting SNe (A. Pastorello et al. 2015b). Strong P Cygni absorption components at about <-300 km s^{-1} are detected for all Fe II lines.

The right panel in Figure C2 displays the evolution of the Ca II $\lambda\lambda$8498, 8542, 8662 lines, possibly blended with O I λ8446. While it is difficult to disentangle these four lines, we find that the bulk velocity of the Ca II + O I complex does not surpass 6000 km s^{-1}. This is the maximum velocity of the red wing of Ca II λ8662. Furthermore, at all epochs past +15 days, narrow P Cygni absorption is observed at a velocity of about -400 km s^{-1}, which continuously decreases to -200 km s^{-1} between +40 and +129 days.

C.8. On SN 2006jc and SN 2011hw

In Figure C3, we show the decomposition of the line profiles of He I λ5876 (left column) and Hα (right column) of three different SNe Ibn: the prototype SN 2006jc, the transitional SN 2011hw, and SN 2021foa 2 weeks after *r*-band maximum. It is clear that our decomposition is in very good agreement with the total line flux of each profile. Furthermore, in contrast to N. Smith et al. (2008, 2012a), we show that our decomposition correctly deblends the Hα and He I λ6678 lines.

In Figure C4, we show the flux-calibrated Hα (red) and He I λ5876 (blue) profiles of SN 2006jc, SN 2011hw and SN 2021foa at ≈ 15 (left panel) and ≈40 (right panel) days *r*-band maximum. These two epochs encompass the line flux ratio plateau observed in Figure 12 for transitional SNe IIn/Ibn. For SN 2006jc, the flux line of Hα is smaller than that of He I in both epochs. This difference is not observed in either SN 2011hw or SN 2021foa, where the line flux ratio is ≈1 for both epochs. Figure C4 proves that the values obtained in A. Reguitti et al. (2022) of the line flux ratio of Hα/He I λ5876, ≈0.5, are not consistent with our observations.

C.9. Line Decomposition in Transitional Objects

For SN 2005la and SN iPTF15akq, a careful analysis was done to take into account the fact that these sources exhibit strong, broad P Cygni absorption profiles for both H and or/He at early epochs. However, we note that this absorption was not accounted for in the line flux calculations.

For SN 2011hw, SN 2005la, SN 2020bqj, and SN 2006jc, we deblended the Hα from the He I λ6678 line by fitting two different Gaussian profiles to each line. This results in line fluxes of Hα and He I λ5876 for SN 2006jc and SN 2011hw that are discrepant by a factor 2 from measurements in the literature (N. Smith et al. 2008, 2012a) using different methods. In Figure C3, we show that our decomposition of the line profiles of Hα and He I λ5876 light recovers the total line flux at ≈2 weeks after maximum.

ORCID iDs

D. Farias https://orcid.org/0000-0002-6886-269X
C. Gall https://orcid.org/0000-0002-8526-3963
G. Narayan https://orcid.org/0000-0001-6022-0484
S. Rest https://orcid.org/0000-0002-3825-0553
V. A. Villar https://orcid.org/0000-0002-5814-4061
C. R. Angus https://orcid.org/0000-0002-4269-7999
K. Auchettl https://orcid.org/0000-0002-4449-9152
K. W. Davis https://orcid.org/0000-0002-5680-4660
R. J. Foley https://orcid.org/0000-0002-2445-5275
A. Gagliano https://orcid.org/0000-0003-4906-8447
J. Hjorth https://orcid.org/0000-0002-4571-2306
L. Izzo https://orcid.org/0000-0001-9695-8472
C. D. Kilpatrick https://orcid.org/0000-0002-5740-7747
H . M. L. Perkins https://orcid.org/0009-0000-5561-9116
E. Ramirez-Ruiz https://orcid.org/0000-0003-2558-3102

C. L. Ransome https://orcid.org/0000-0003-4175-4960
A. Sarangi https://orcid.org/0000-0002-9820-679X
R. Yarza https://orcid.org/0000-0003-0381-1039
D. A. Coulter https://orcid.org/0000-0003-4263-2228
D. O. Jones https://orcid.org/0000-0002-6230-0151
N. Khetan https://orcid.org/0000-0003-2720-8904
A. Rest https://orcid.org/0000-0002-4410-5387
M. R. Siebert https://orcid.org/0000-0003-2445-3891
J. J. Swift https://orcid.org/0000-0002-9486-818X
K. Taggart https://orcid.org/0000-0002-5748-4558
S. Tinyanont https://orcid.org/0000-0002-1481-4676
P. Wrubel https://orcid.org/0009-0009-2891-9151
T. J. L. de Boer https://orcid.org/0000-0001-5486-2747
K. E. Clever https://orcid.org/0000-0001-8756-1262
A. Dhara https://orcid.org/0000-0002-5950-1702
H. Gao https://orcid.org/0000-0003-1015-5367
C.-C. Lin https://orcid.org/0000-0002-7272-5129

References

Alam, S., Albareti, F. D., Allende Prieto, C., et al. 2015, ApJS, 219, 12
Aleo, P. D., Malanchev, K., Sharief, S., et al. 2023, ApJS, 266, 9
Anderson, J. P., Dessart, L., Gutierrez, C. P., et al. 2014, MNRAS, 441, 671
Andrews, J. E., Smith, N., McCully, C., et al. 2017, MNRAS, 471, 4047
Angus, C. 2021, TNSCR, 2021-1133, 1
Astropy Collaboration, Price-Whelan, A. M., Sipőcz, B. M., et al. 2018, AJ, 156, 123
Astropy Collaboration, Robitaille, T. P., Tollerud, E. J., et al. 2013, A&A, 558, A33
Ben-Ami, T., Arcavi, I., Newsome, M., et al. 2023, ApJ, 946, 30
Bevan, A., & Barlow, M. J. 2016, MNRAS, 456, 1269
Bevan, A. M., Krafton, K., Wesson, R., et al. 2020, ApJ, 894, 111
Bilinski, C., Smith, N., Williams, G. G., et al. 2020, MNRAS, 498, 3835
Boian, I., & Groh, J. H. 2018, A&A, 617, A115
Brennan, S. J., Fraser, M., Johansson, J., et al. 2022a, MNRAS, 513, 5666
Brennan, S. J., Fraser, M., Johansson, J., et al. 2022b, MNRAS, 513, 5642
Brennan, S. J., Schulze, S., Lunnan, R., et al. 2024b, A&A, 690, A259
Brennan, S. J., Sollerman, J., Irani, I., et al. 2024a, A&A, 684, L18
Brown, P. J., Kuin, P., Scalzo, R., et al. 2014, ApJ, 787, 29
Brown, T. M., Baliber, N., Bianco, F. B., et al. 2013, PASP, 125, 1031
Chatzopoulos, E., Wheeler, J. C., & Vinko, J. 2012, ApJ, 746, 121
Chatzopoulos, E., Wheeler, J. C., Vinko, J., Horvath, Z. L., & Nagy, A. 2013, ApJ, 773, 76
Chevalier, R. A. 1976, ApJ, 207, 872
Childress, M. J., Vogt, F. P. A., Nielsen, J., & Sharp, R. G. 2014, Ap&SS, 349, 617
Chugai, N. N. 2009, MNRAS, 400, 866
Chugai, N. N. 2018, MNRAS, 481, 3643
Clemens, J. C., Crain, J. A., & Anderson, R. 2004, Proc. SPIE, 5492, 331
Cold, C., & Hjorth, J. 2023, A&A, 670, A48
Coulter, D. A., Jones, D. O., McGill, P., et al. 2022, YSE-PZ: An Open-source Target and Observation Management System, v0.3.0, Zenodo, doi:10.5281/zenodo.7278430
Coulter, D. A., Jones, D. O., McGill, P., et al. 2023, PASP, 135, 064501
Cushing, M. C., Vacca, W. D., & Rayner, J. T. 2004, PASP, 116, 362
Davis, K. W., Taggart, K., Tinyanont, S., et al. 2023, MNRAS, 523, 2530
Dessart, L., Audit, E., & Hillier, D. J. 2015, MNRAS, 449, 4304
Dessart, L., & Hillier, D. J. 2022, A&A, 660, L9
Dessart, L., Hillier, D. J., & Kuncarayakti, H. 2022, A&A, 658, A130
Dong, Y., Tsuna, D., Valenti, S., et al. 2024, arXiv:2405.04583
Dopita, M., Hart, J., McGregor, P., et al. 2007, Ap&SS, 310, 255
Drout, M. R., Soderberg, A. M., Gal-Yam, A., et al. 2011, ApJ, 741, 97
Earl, N., Tollerud, E., O'Steen, R., et al. 2023, astropy/specutils: v1.12.0, Zenodo, doi:10.5281/zenodo.10016569
Elias-Rosa, N., Pastorello, A., Benetti, S., et al. 2016, MNRAS, 463, 3894
Flewelling, H. A., Magnier, E. A., Chambers, K. C., et al. 2020, ApJS, 251, 7
Foley, R. J., Berger, E., Fox, O., et al. 2011, ApJ, 732, 32
Foley, R. J., Smith, N., Ganeshalingam, M., et al. 2007, ApJL, 657, L105
Fox, O., Skrutskie, M. F., Chevalier, R. A., et al. 2009, ApJ, 691, 650
Fransson, C., Ergon, M., Challis, P. J., et al. 2014, ApJ, 797, 118
Fransson, C., Sollerman, J., Strotjohann, N. L., et al. 2022, A&A, 666, A79
Fraser, M. 2020, RSOS, 7, 200467
Fraser, M., Inserra, C., Jerkstrand, A., et al. 2013, MNRAS, 433, 1312
Freudling, W., Romaniello, M., Bramich, D. M., et al. 2013, A&A, 559, A96
Gall, C., & Hjorth, J. 2018, ApJ, 868, 62
Gall, C., Hjorth, J., & Andersen, A. C. 2011, A&ARv, 19, 43
Gall, C., Hjorth, J., Rosswog, S., Tanvir, N. R., & Levan, A. J. 2017, ApJL, 849, L19
Gall, C., Hjorth, J., Watson, D., et al. 2014, Natur, 511, 326
Gal-Yam, A., Bruch, R., Schulze, S., et al. 2022, Natur, 601, 201
Gal-Yam, A., Leonard, D. C., Fox, D. B., et al. 2007, ApJ, 656, 372
Gan, W.-P., Wang, S.-Q., & Liang, E.-W. 2021, ApJ, 914, 125
Gangopadhyay, A., Dukiya, N., Moriya, T. J., et al. 2024, arXiv:2409.02666
Gangopadhyay, A., Misra, K., Hiramatsu, D., et al. 2020, ApJ, 889, 170
Gangopadhyay, A., Misra, K., Hosseinzadeh, G., et al. 2022, ApJ, 930, 127
Guillochon, J., Nicholl, M., Villar, V. A., et al. 2018, ApJS, 236, 6
Gutiérrez, C. P., Anderson, J. P., Hamuy, M., et al. 2017, ApJ, 850, 89
Harris, C. R., Millman, K. J., van der Walt, S. J., et al. 2020, Natur, 585, 357
Hildebrand, R. H. 1983, QJRAS, 24, 267
Hiramatsu, D., Matsumoto, T., Berger, E., et al. 2024, ApJ, 964, 181
Hosseinzadeh, G., Arcavi, I., Valenti, S., et al. 2017, ApJ, 836, 158
Hosseinzadeh, G., McCully, C., Zabludoff, A. I., et al. 2019, ApJL, 871, L9
Hunter, J. D. 2007, CSE, 9, 90
Jones, D. O., Foley, R. J., Narayan, G., et al. 2021, ApJ, 908, 143
Karamehmetoglu, E., Taddia, F., Sollerman, J., et al. 2017, A&A, 602, A93
Kilpatrick, C. D., Foley, R. J., Drout, M. R., et al. 2018, MNRAS, 473, 4805
Kool, E. C., Karamehmetoglu, E., Sollerman, J., et al. 2021, A&A, 652, A136
Kumar, B., Eswaraiah, C., Singh, A., et al. 2019, MNRAS, 488, 3089
Leonard, D. C., Filippenko, A. V., Barth, A. J., & Matheson, T. 2000, ApJ, 536, 239
Liu, Y.-Q., Modjaz, M., Bianco, F. B., & Graur, O. 2016, ApJ, 827, 90
Lucy, L. B., Danziger, I. J., Gouiffes, C., & Bouchet, P. 1989, in IAU Coll. 120: Structure and Dynamics of the Interstellar Medium Vol. 350, ed. G.Tenorio-Tagle, M. Moles, & J. Melnick (Berlin: Springer), 164
Maeda, K., & Moriya, T. J. 2022, ApJ, 927, 25
Margutti, R., Milisavljevic, D., Soderberg, A. M., et al. 2014, ApJ, 780, 21
Mauerhan, J., & Smith, N. 2012, MNRAS, 424, 2659
Mauerhan, J., Williams, G. G., Smith, N., et al. 2014, MNRAS, 442, 1166
Mauerhan, J. C., Smith, N., Filippenko, A. V., et al. 2013, MNRAS, 430, 1801
Maund, J. R., Pastorello, A., Mattila, S., Itagaki, K., & Boles, T. 2016, ApJ, 833, 128
McCully, C., Volgenau, N. H., Harbeck, D.-R., et al. 2018, Proc. SPIE, 10707, 107070K
Miller, J. S., & Stone, R. P. S. 1993, 66
Morozova, V., Piro, A. L., & Valenti, S. 2018, ApJ, 858, 15
Nicholl, M. 2018, RNAAS, 2, 230
Nicholl, M., Guillochon, J., & Berger, E. 2017, ApJ, 850, 55
Nyholm, A., Sollerman, J., Taddia, F., et al. 2017, A&A, 605, A6
Nyholm, A., Sollerman, J., Tartaglia, L., et al. 2020, A&A, 637, A73
Ofek, E. O., Lin, L., Kouveliotou, C., et al. 2013a, ApJ, 768, 47
Ofek, E. O., Sullivan, M., Cenko, S. B., et al. 2013b, Natur, 494, 65
Pastorello, A., Benetti, S., Brown, P. J., et al. 2015a, MNRAS, 449, 1921
Pastorello, A., Cappellaro, E., Inserra, C., et al. 2013, ApJ, 767, 1
Pastorello, A., Hadjiyska, E., Rabinowitz, D., et al. 2015b, MNRAS, 449, 1954
Pastorello, A., Kochanek, C. S., Fraser, M., et al. 2018, MNRAS, 474, 197
Pastorello, A., Mattila, S., Zampieri, L., et al. 2008a, MNRAS, 389, 113
Pastorello, A., Quimby, R. M., Smartt, S. J., et al. 2008b, MNRAS, 389, 131
Pastorello, A., Smartt, S. J., Mattila, S., et al. 2007, Natur, 447, 829
Patat, F., Taubenberger, S., Benetti, S., Pastorello, A., & Harutyunyan, A. 2011, A&A, 527, L6
Pellegrino, C., Howell, D. A., Terreran, G., et al. 2022, ApJ, 938, 73
Pellegrino, C., Modjaz, M., Takei, Y., et al. 2024, arXiv:2407.18291
Planck Collaboration, Ade, P. A. R., Aghanim, N., et al. 2014, A&A, 571, A16
Rayner, J. T., Toomey, D. W., Onaka, P. M., et al. 2003, PASP, 115, 362
Reguitti, A., Pastorello, A., Pignata, G., et al. 2022, A&A, 662, L10
Reguitti, A., Pignata, G., Pastorello, A., et al. 2024, A&A, 686, A231
Rest, A., Stubbs, C., Becker, A. C., et al. 2005, ApJ, 634, 1103
Rest, S., Rest, A., Kilpatrick, C. D., et al. 2024, arXiv:2405.03747
Rest, S., Rest, A., Wang, Q., et al. 2023, ATClean: High-Fidelity, Statistically Clean ATLAS Light Curves and Feature Detection, v2, Zenodo, doi:10.5281/zenodo.7897346
Roming, P. W. A., Kennedy, T. E., Mason, K. O., et al. 2005, SSRv, 120, 95
Rouleau, F., & Martin, P. G. 1991, ApJ, 377, 526
Schechter, P. L., Mateo, M., & Saha, A. 1993, PASP, 105, 1342
Schlafly, E. F., & Finkbeiner, D. P. 2011, ApJ, 737, 103
Schlegel, E. M. 1990, MNRAS, 244, 269
Shivvers, I., Zheng, W., Van Dyk, S. D., et al. 2017, MNRAS, 471, 4381
Siebert, M. R., Foley, R. J., Jones, D. O., et al. 2019, MNRAS, 486, 5785
Smartt, S. J. 2009, ARA&A, 47, 63

Smith, N. 2017, in Handbook of Supernovae, ed. A. W. Alsabti & P. Murdin (Berlin: Springer), 403
Smith, N., & Andrews, J. E. 2020, MNRAS, 499, 3544
Smith, N., Andrews, J. E., Filippenko, A. V., et al. 2022, MNRAS, 515, 71
Smith, N., Foley, R. J., & Filippenko, A. V. 2008, ApJ, 680, 568
Smith, N., Li, W., Miller, A. A., et al. 2011, ApJ, 732, 63
Smith, N., Mauerhan, J. C., Cenko, S. B., et al. 2015, MNRAS, 449, 1876
Smith, N., Mauerhan, J. C., & Prieto, J. L. 2013, MNRAS, 438, 1191
Smith, N., Mauerhan, J. C., Silverman, J. M., et al. 2012a, MNRAS, 426, 1905
Smith, N., Silverman, J. M., Filippenko, A. V., et al. 2012b, AJ, 143, 17
Speagle, J. S. 2020, MNRAS, 493, 3132
Stanek, K. Z., & Kochanek, C. S. 2021, TNSTR, 2021-767, 1
Strotjohann, N. L., Ofek, E. O., Gal-Yam, A., et al. 2021, ApJ, 907, 99
Sun, N.-C., Maund, J. R., Hirai, R., Crowther, P. A., & Podsiadlowski, P. 2020, MNRAS, 491, 6000
Swift, J. J., Andersen, K., Arculli, T., et al. 2022, PASP, 134, 035005
Taddia, F., Stritzinger, M. D., Fransson, C., et al. 2020, A&A, 638, A92
Thöne, C. C., de Ugarte Postigo, A., Leloudas, G., et al. 2017, A&A, 599, A129
Thornton, I., & Villar, V. A. 2022, villrv/extrabol, v1.0.0, Zenodo, doi:10.5281/zenodo.7261669
Tonry, J. L., Denneau, L., Heinze, A. N., et al. 2018, PASP, 130, 064505
Turatto, M., Benetti, S., & Cappellaro, E. 2003, in From Twilight to Highlight: The Physics of Supernovae, ed. W. Hillebrandt & B. Leibundgut (Berlin: Springer), 200
Vacca, W. D., Cushing, M. C., & Rayner, J. T. 2003, PASP, 115, 389
Vernet, J., Dekker, H., D'Odorico, S., et al. 2011, A&A, 536, A105
Villar, V. A., Berger, E., Metzger, B. D., & Guillochon, J. 2017, ApJ, 849, 70
Wang, Q., Goel, A., Dessart, L., et al. 2024, MNRAS, 530, 3906
Wang, S.-Q., & Li, L. 2020, ApJ, 900, 83